The JPL lunar gravity field to spherical harmonic degree 660 from the GRAIL Primary Mission

Citation: Konopliv, Alex S., Ryan S. Park, Dah-Ning Yuan, Sami W. Asmar, Michael M. Watkins, James G. Williams, Eugene Fahnestock, et al. "The JPL Lunar Gravity Field to Spherical Harmonic Degree 660 from the GRAIL Primary Mission." Journal of Geophysical Research: Planets 118, no. 7 (July 2013): 1415–1434.

As Published: http://dx.doi.org/10.1002/jgre.20097

Publisher: American Geophysical Union

Persistent URL: http://hdl.handle.net/1721.1/85858

Version: Final published version: final published article, as it appeared in a journal, conference proceedings, or other formally published context

The JPL lunar gravity field to spherical harmonic degree 660 from the GRAIL Primary Mission

Alex S. Konopliv,[1] Ryan S. Park,[1] Dah-Ning Yuan,[1] Sami W. Asmar,[1] Michael M. Watkins,[1] James G. Williams,[1] Eugene Fahnestock,[1] Gerhard Kruizinga,[1] Meegyeong Paik,[1] Dmitry Strekalov,[1] Nate Harvey,[1] David E. Smith,[2] and Maria T. Zuber[2]

Received 1 March 2013; revised 13 May 2013; accepted 16 May 2013; published 9 July 2013.

[1] The lunar gravity field and topography provide a way to probe the interior structure of the Moon. Prior to the Gravity Recovery and Interior Laboratory (GRAIL) mission, knowledge of the lunar gravity was limited mostly to the nearside of the Moon, since the farside was not directly observable from missions such as Lunar Prospector. The farside gravity was directly observed for the first time with the SELENE mission, but was limited to spherical harmonic degree $n \leq 70$. The GRAIL Primary Mission, for which results are presented here, dramatically improves the gravity spectrum by up to ~4 orders of magnitude for the entire Moon and for more than 5 orders-of-magnitude over some spectral ranges by using interspacecraft measurements with near 0.03 μm/s accuracy. The resulting GL0660B ($n = 660$) solution has 98% global coherence with topography to $n = 330$, and has variable regional surface resolution between $n = 371$ (14.6 km) and $n = 583$ (9.3 km) because the gravity data were collected at different spacecraft altitudes. The GRAIL data also improve low-degree harmonics, and the uncertainty in the lunar Love number has been reduced by ~5× to $k_2 = 0.02405 \pm 0.00018$. The reprocessing of the Lunar Prospector data indicates ~3× improved orbit uncertainty for the lower altitudes to ~10 m, whereas the GRAIL orbits are determined to an accuracy of 20 cm.

Citation: Konopliv, A. S., et al. (2013), The JPL lunar gravity field to spherical harmonic degree 660 from the GRAIL Primary Mission, *J. Geophys. Res. Planets*, *118*, 1415–1434, doi:10.1002/jgre.20097.

1. Introduction

[2] The measurement of the lunar gravity field has been a goal from the beginning of the space program when the Soviet Luna 10 mission in 1966 determined a fairly accurate estimate of the gravitational oblateness or J_2 spherical harmonic coefficient [*Akim*, 1966] from long arc analysis of the mission's 460 orbits. Soon after in 1967, short arc line-of-sight analysis of Lunar Orbiter V tracking data showed large nearside gravity anomalies or "mascons" (mass concentrations) over the maria-filled impact basins [*Muller and Sjogren*, 1968]. Noted were the five large nearside mascons within Maria Imbrium, Serenitatis, Crisium, Nectaris, and Humorum, and Mare Orientale near the limb. In total, five Lunar Orbiter spacecraft from 1966 to 1968 provided Deep Space Network (DSN) Doppler tracking data to map the lunar gravity field with orbital inclinations from near equatorial to near polar for the last two missions. Two Apollo missions 15 and 16 followed in 1971 and 1972 with two small spin-stabilized subsatellites that were released from the Command Service Module. Both spacecraft had S-band transponders and were tracked by the DSN, but did not have any propulsion system to adjust the orbit. After both were released in a 100 km nearly circular orbit, the Apollo 15 subsatellite lasted for several years whereas the Apollo 16 subsatellite surprisingly (at that time) impacted the lunar surface after only 35 days. The difference in long-term orbit behavior is attributable to the initial inclination of the orbit, leading to short lifetimes of any low, circular 10° inclination orbit (Apollo 16) and longer lifetimes for 30° inclination orbits (Apollo 15). If the five large nearside mascons did not exist, the Apollo 16 orbit lifetime would have been much longer and similar to Apollo 15, and fuel usage for any polar orbiter such as Lunar Prospector (LP) and Gravity Recovery and Interior Laboratory (GRAIL) would have been greatly reduced.

[3] Many gravity analyses were performed with the historic data sets, but with limited spherical harmonic resolution to at most degree 16 [*Bills and Ferrari*, 1980]. The development of higher-resolution gravity fields began after recovery of the historic Lunar Orbiter and Apollo data sets, and the arrival of faster computers. The new higher resolution fields to degree 60 [*Konopliv et al.*, 1993] showed improved spherical harmonic resolution and for the first time accurately

[1]Jet Propulsion Laboratory, California Institute of Technology, Pasadena, California, USA.
[2]Department of Earth, Atmospheric and Planetary Sciences, Massachusetts Institute of Technology, Cambridge, Massachusetts, USA.

Corresponding author: A. S. Konopliv, Jet Propulsion Laboratory, California Institute of Technology, Pasadena, CA, USA. (Alexander.S.Konopliv@jpl.nasa.gov)

2169-9097/13/10.1002/jgre.20097

predicted long-term orbit behavior such as that of the Apollo subsatellites. The Clementine mission at a higher 400 km altitude in 1994 further improved the low-degree coefficients of the gravity field [*Zuber et al*., 1994; *Lemoine et al*., 1997].

[4] The next major improvement in the lunar gravity field occurred with the Lunar Prospector Discovery mission's arrival at the Moon in 1998 (a 75th degree and order field LP75G [*Konopliv et al*., 1998]). In addition, the LP degree-2 and -3 harmonics together with the Lunar Laser Ranging data (LLR) [see *Dickey et al*., 1994] improved the moments of inertia of the Moon by about fivefold. A simple spin-stabilized spacecraft with limited propulsive maneuvers ideal for gravity, LP provided 1 year of continuous S-band tracking at an average 100 km polar altitude, and 1 and 6 months of a lower mean altitude of 40 and 30 km, respectively. Subsequently, higher-resolution models based upon LP data to degrees 100 (LP100J) [*Konopliv et al*., 2001, *Carranza et al*., 1999] and ultimately degree 150 (LP150Q), especially improved the higher-latitude (beyond 30°) not yet sampled nearside regions of the Moon and revealed many new mascons. LP150Q was often used as the initial operational gravity field for later missions to the Moon including GRAIL. Comparable lunar gravity fields were also developed using the same historical and LP data (degree 150 GLGM-3) [*Mazarico et al*., 2010], and by applying regional constraint techniques to extract more nearside high-frequency gravity [*Han et al*., 2011].

[5] Although the LP spacecraft provides strong gravity information as a low-altitude, spin-stabilized proof mass in orbit with long periods of time (several weeks) between maneuvers, it can only provide limited information on the lunar farside gravity due to the lack of direct tracking data from the Earth. Using LP data together with Lunar Orbiter and Apollo subsatellites, the crisscrossing of orbit groundtracks over the lunar farside and the corresponding integrated effect on the orbit shows the existence of lunar farside mascons, but only partially resolved as a central gravity high with a negative ring [*Konopliv et al*., 2001]. As individual coefficients, the gravity field is determined globally to about degree 15. No direct measurement of the lunar farside gravity occurred until the SELENE mission with a four-way Doppler relay that measured the motion of the main 100 km altitude polar orbiting Kaguya spacecraft through a higher-altitude relay satellite redirected to Earth ground stations [*Namiki et al*., 2009]. The corresponding resolution of the SELENE gravity fields [100th-degree fields SGM100h, *Matsumoto et al*., 2010, and a follow-on SGM100i, *Goossens et al*., 2011], extracted farside information up to about harmonic degree 70. SELENE showed farside gravity clearly including mascons for the first time.

[6] For development of the lunar gravity field, all the previous missions including LP and SELENE are limited to the S-band quality of the Doppler data, typically measuring the line-of-sight spacecraft velocity to 0.3 mm/s or 300 μm/s. Based upon the Earth Gravity Recovery and Climate Experiment (GRACE) mission [*Tapley et al*., 2004a], the GRAIL mission [*Zuber et al*., 2013a] uses two spacecraft flying in formation [*Roncoli and Fujii*, 2010] to provide the first highly accurate measurement of both the lunar nearside and farside gravity field. The prelaunch requirement for interspacecraft Ka-band measurement accuracy had red-noise characteristics varying between 0.4 μm/s (0.4×10^{-6} m/s) for long wavelengths to 1.0 μm/s for the shorter wavelengths corresponding to 5 s data sample times, or a mean of 0.50 μm/s overall [*Park et al*., 2012; *Asmar et al*., 2013]. As we will display below, the realized GRAIL Ka-band measurement accuracy is more than 10 times better than these requirements, with noise of about 0.03 μm/s. Compared to the previous S-band missions, this provides a stunning 4 orders-of-magnitude improvement in measurement of the spacecraft along-track velocity.

[7] Once the interspacecraft data are processed, the resulting GRAIL gravity field [*Zuber et al*., 2013b] shows 4 to 5 orders-of-magnitude improvement at degrees and orders that sample the major lunar basins and 98% coherence with topography to harmonic degree 330, and provides a new view of the lunar interior such as crustal fractures likely from an early thermal expansion of the Moon [*Andrews-Hanna et al*., 2013] and indicates lower crustal density and higher porosity than expected [*Wieczorek et al*., 2013]. Two independent but collaborative groups at the Jet Propulsion Laboratory (JPL, this paper) and Goddard Space Flight Center (GSFC) [*Lemoine et al*., 2013] have determined the lunar gravity field from the GRAIL data. The results are comparable, validate the gravity fields, and help characterize their uncertainties. The initial GRAIL lunar gravity field [*Zuber et al*., 2013b] was a global field to degree and order 420 (half-wavelength surface resolution = 13 km). This paper presents the gravity development procedure and extends the resolution to degree and order 660 (half-wavelength surface resolution = 8.3 km). However, analysis is still limited to the higher-altitude (55 km average) Primary Mission (PM). The local resolution of the gravity field is dependent upon the spacecraft altitude and the average global resolution for the GRAIL primary mission is near degree 420. The Bouguer anomaly resolution (gravity minus gravity from topography) is closer to degree 330 (half-wavelength surface resolution = 18.2 km) [*Wieczorek et al*., 2013].

2. Mission and Orbit Design Considerations

[8] The twin GRAIL spacecraft (Figure 1), Ebb (GRAIL-A) and Flow (GRAIL-B), were launched on 10 September 2011 and, using a low-energy transfer orbit, individually arrived at the Moon on 31 December 2011 and 1 January 2012. The extra three months of transfer time, versus the direct transfer time of 3 to 6 days, not only gave significant fuel savings and thus lower mission cost [*Roncoli and Fujii*, 2010], but allowed the spacecraft to stabilize nongravitational forces due to outgassing of painted surfaces or volatiles remaining on the spacecraft or within its structure subsequent to launch. During a test of the GRAIL measurement system during cruise on 22 September 2011, strong outgassing ($\sim10^{-10}$ km/s^2) was observed as parts of the spacecraft were exposed to the Sun for the first time. LP, which used a direct transfer to the Moon, experienced similar outgassing that affected the first several weeks of lunar orbit [*Konopliv et al*., 1999].

[9] The GRAIL science mission began 2 months after arrival at the Moon and 1 week earlier than initially planned. The 3 month Primary Mission of gravity mapping began 1 March 2012 and ended 29 May 2012, and these dates were defined by the geometry of the orbit and the power requirements of the spacecraft. The GRAIL spacecraft had body-fixed solar arrays that remained in the plane of the orbit

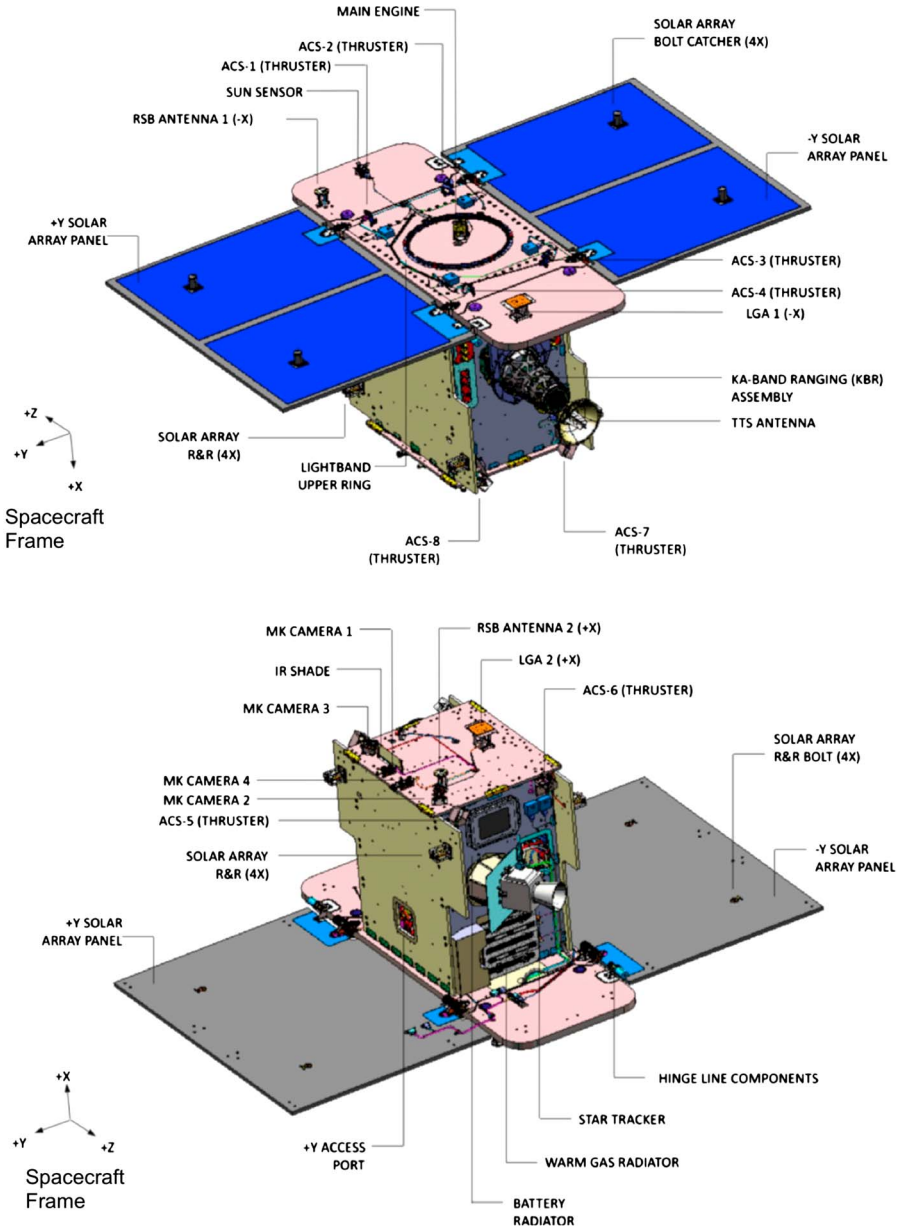

Figure 1. The GRAIL-B (Flow) spacecraft. The Sun-facing direction shows the solar arrays (blue) and a specially designed bus cover (pink) to limit exposure of the bus to the Sun and thus errors in the nongravitational accelerations.

during science data collection. For this reason, the spacecraft had insufficient power to collect science data for times when the angle between the orbit plane and the Sun direction, or solar beta angle, is <49° [*Roncoli and Fujii*, 2010]. After the PM, the next favorable geometry was the extended mission from 30 August 2012 to the end of mission on 14 December 2012. The gravity development results presented in this paper are for the PM only (~55 km average altitude), and future studies will address the higher-resolution (~23 km average altitude) extended mission data.

[10] Once at the Moon, the spacecraft were placed in near-polar circular orbits with an initial separation distance of 80 km in the along-track direction and 113 min periods. The inclination varied by 1.2° as shown by Figure 2, with the mean inclination 89.2° chosen as a trade-off between minimizing the data tracking gap at the poles (higher inclination), and providing better dynamical determination of the low-degree gravity field (lower inclination). The inclinations of the two spacecraft match to better than 0.0001°, and the resulting polar gap at the conclusion of the PM is 1.5 km, far below the half-wavelength resolution of a degree-660 gravity field (8.3 km).

[11] The separation distance between the spacecraft (Figure 3) was chosen to optimize different aspects of the gravity field. The long wavelength components of the gravity field, including tides and possible time-varying inner core motion [*Williams*, 2007], are best determined (~2–4 times better) using the largest spacecraft separation distances, since there is less cancellation of near common mode intersatellite range changes. This assumes the range measurement accuracy is

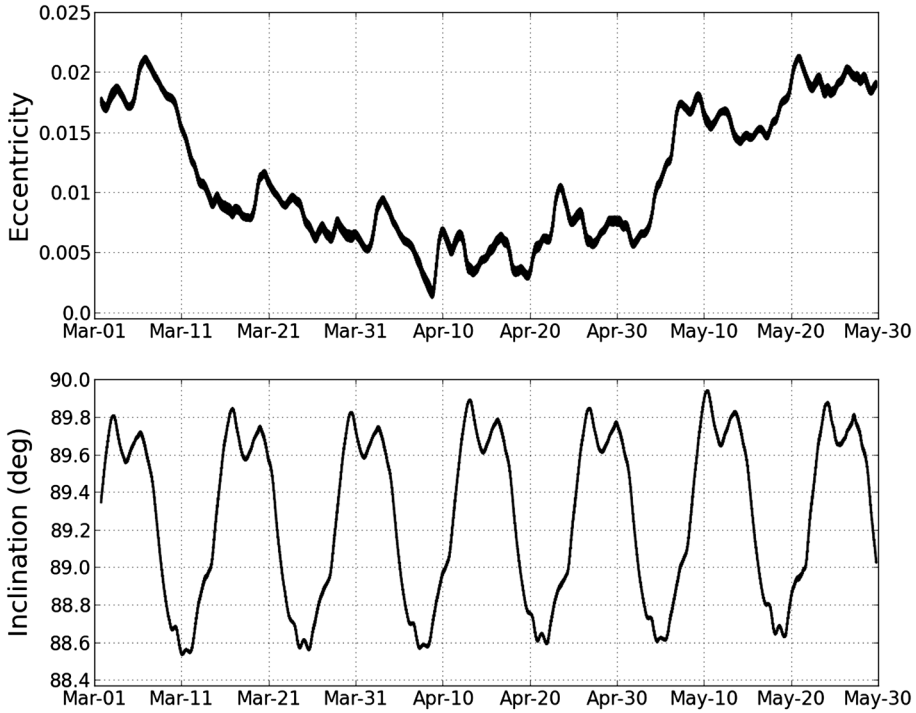

Figure 2. The GRAIL spacecraft orbit eccentricity and near-polar inclination. The bimonthly oscillation in the inclination is due to the C_{22} gravity coefficient.

not degraded by reduced signal strength (no degradation is observed for GRAIL at larger separation distances). The high-frequency content of the gravity field is not as sensitive to the spacecraft separation, but still prefers longer separations as well. The limiting factor for choosing the spacecraft separation is the possible reflection of the Ka-band range signals off the lunar surface (i.e., multipath) that might degrade the interspacecraft range and range-rate accuracy. The separation

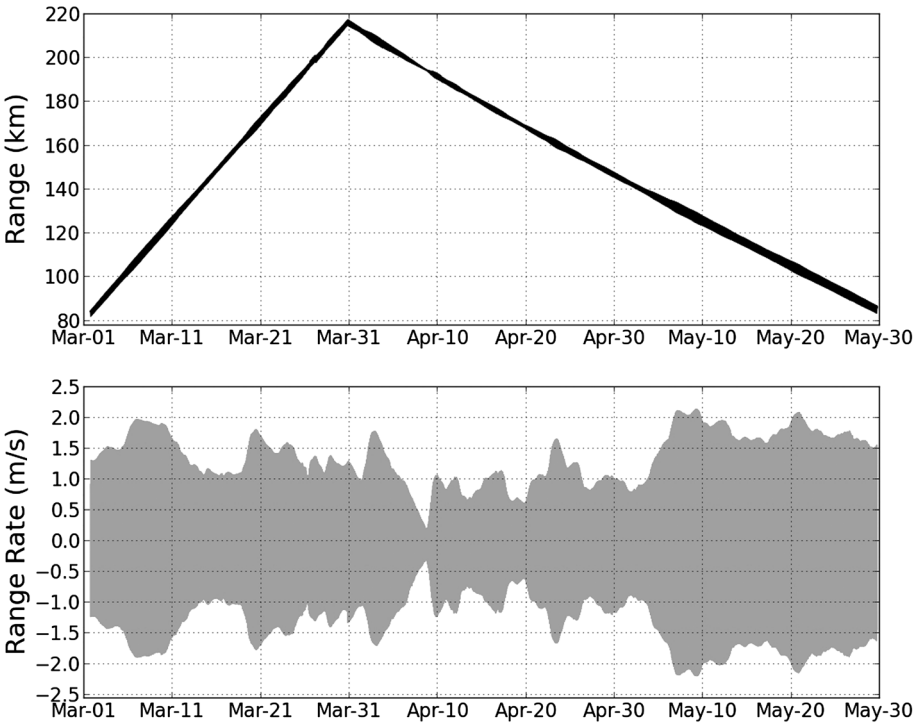

Figure 3. The separation distance and relative velocity between the GRAIL spacecraft from begin of Primary Mission (1 March 2012) to end of the Primary Mission (29 May 2012). The relative velocity is dominated by large oscillations with period equal to the orbit period, which is much larger than the average interspacecraft drift rate.

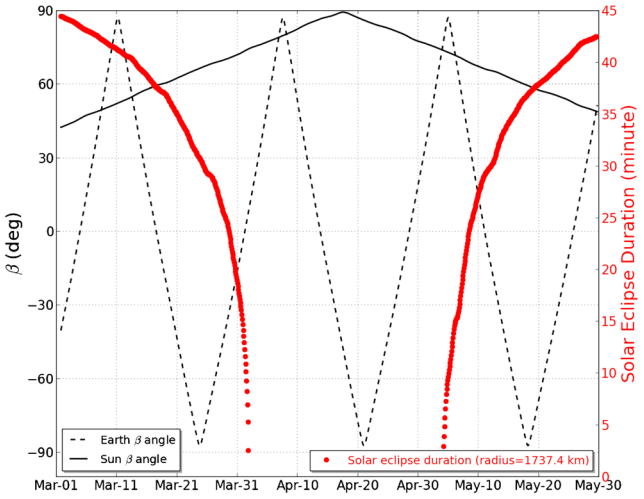

Figure 4. Geometry for the GRAIL Primary Mission as viewed from the Sun and Earth. A 90° β-angle indicates the spacecraft orbit plane and solar arrays are normal to the Sun direction. During the middle 30 days of the PM, the GRAIL spacecraft are in full Sun at all times. This minimizes the nongravitational forces on the spacecraft and provides the best data for determination of the long wavelength gravity features. The Earth β-angle shows when the orbit plane is edge-on (0°) and face-on (90°, −90°) when viewed from Earth.

distance was therefore chosen to be as large as possible without the measurement degradation due to multipath.

[12] A constant separation distance results in degradation of the gravity field for wavelengths equal to the separation distance, since both spacecraft experience effects of that wavelength at the same time and that wavelength has a smaller signal in the biased-range measurement between the spacecraft. This resonance occurs for harmonic degree $n = 360/(\Delta/30.3) = 2\pi R/\Delta$ where Δ is the spacecraft separation in kilometers and $\Delta/30.3$ is the separation distance in degrees and R is the lunar radius. For this reason, the spacecraft distance was designed to drift from a closer 80 km distance at the lower altitudes at the beginning of the mission to a 220 km separation at higher altitudes, and back to 80 km. Without this variable distance, the resonance at 220 km separation would occur at harmonic degrees 49, 98, and 147, etc., and for the minimum 80 km separation, the resonance occurs later, starting at degree 135. The largest separation distance occurs during the central part of the mission at higher altitude and is ideal for determination of the longer-wavelength tide and possible time variable inner core periodic signatures in the gravity field [*Williams*, 2007]. The spacecraft nongravitational forces are also minimized during this part of the mission due to full Sun on the spacecraft uninterrupted by eclipses (see Figure 4).

[13] Spacecraft altitude is the most important consideration for the expected resolution of the gravity field. The selection of the Primary Mission mean altitude (55 km) allowed GRAIL to far exceed the science requirement to determine a 180th degree spherical harmonic field [*Zuber et al.*, 2013a]. At this altitude, spacecraft maneuvers to maintain the orbit altitude during the PM were not needed, and only one maneuver on 30 March 2012 was performed on GRAIL-B to change the spacecraft separation from drifting apart to coming together. Smaller propulsive maneuvers using the Attitude Control System thrusters occurred about every 2 days to reduce momentum in the Reaction Wheel Assembly. The orbits at beginning and end of the PM had higher eccentricity and thus lower periapse altitudes (Figure 5) and provide the highest localized resolution of the gravity field. The final distribution of minimum spacecraft altitude over the surface shows mostly a near equatorial periapse band (Figure 6).

3. Gravity Measurement Data

[14] The detection of the lunar gravity field is achieved by observing the effect of the gravity field on the motion of each GRAIL spacecraft as it orbits the Moon. The entire spacecraft, in essence, is the instrument used to measure the gravity field [*Asmar et al.*, 2013] once accounting for all other nongravitational forces acting on the spacecraft. The three measurement types for the GRAIL mission are DSN two-way S-band Doppler, DSN one-way X-band Doppler, and instantaneous interspacecraft Ka-band range-rate (KBRR) data, which is derived from time differentiation of the biased-range (phase) Ka-band data. Table 1 summarizes the number of measurements used for GRAIL gravity development. The DSN data determine the absolute position of the spacecraft orbit and are analogous to the GPS measurements for the GRACE mission. Each GRAIL spacecraft has two pairs of low-gain antennas (LGA), two X-band and two S-band antenna locations, that are used for DSN tracking. The selection of the LGA depends on the orbit geometry relative to Earth.

[15] The primary science instrument on each GRAIL spacecraft was the Lunar Gravity Ranging System (LGRS), which maintained a carrier-only radio link between the two spacecraft at Ka-band frequency [*Klipstein et al.*, 2013]. The LGRS Ka-carrier frequency and the LGRS timing clock were derived from an Ultra Stable Oscillator (USO). The same USO was used by the Time Transfer System (TTS) to generate ranging code modulated on an S-band carrier to sync the relative timing between the two LGRS clocks, which ensured that the Ka ranging accuracy requirement

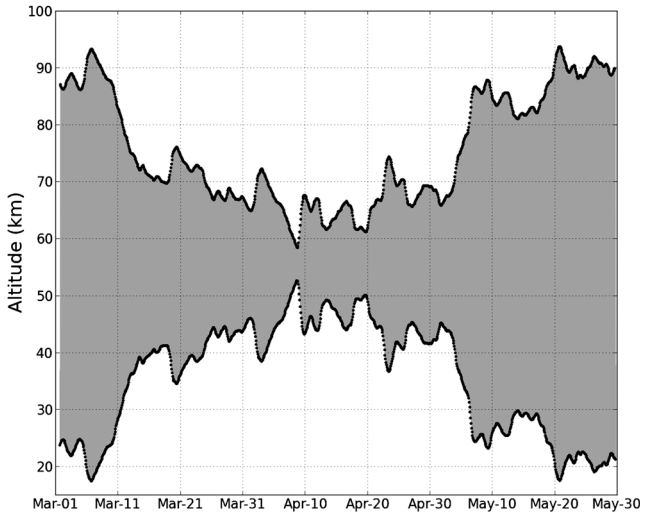

Figure 5. Spacecraft periapse and apoapse altitudes during the Primary Mission.

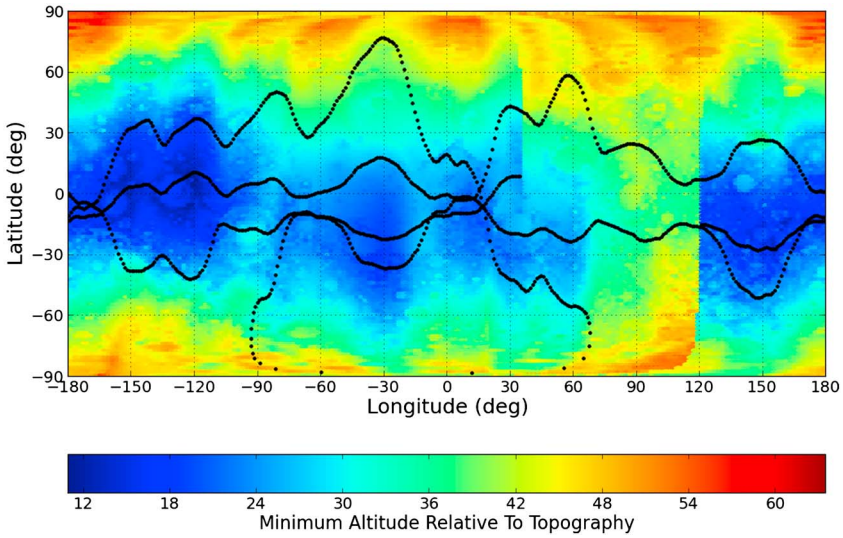

Figure 6. Minimum spacecraft altitude (in km) over the actual surface topography of the Moon [*Smith et al.*, 2010] at the conclusion of the Primary Mission. The black dots indicate the history of periapse locations.

was achieved. The twin spacecraft also had a carrier-only Radio Science Beacon (RSB) at X-band frequency, which was derived from the USO as well. The RSB X-band one-way Doppler measurement from the GRAIL spacecraft to a DSN station is used in the orbit determination process and it is also used to measure the USO frequency. The USO frequency then scales the LGRS Ka-carrier range measurement.

[16] The relative timing alignment between the two LGRS clocks plays an important role in forming the intersatellite one-way phase measurement in both directions. Adding the Ka-band phase measurements from both spacecraft eliminates most LGRS clock errors, provided the LGRS clocks are aligned to better than 10^{-7} s in a bias sense and the variability about this bias is less than 90×10^{-12} s [*Kruizinga et al.*, 2013].

[17] Initially, the GRAIL absolute timing system relied on time correlations between the LGRS clock and the spacecraft clock, which in turn was correlated with UTC based on time correlation packets. These time correlation packets were transmitted once every 10 min when a DSN station was tracking the spacecraft at S-band. Time correlation packets provide a biased measurement of the absolute LGRS clock and suffer systematic errors including unknown electronic delays and limited precision, which resulted in an overall accuracy of 10^{-2} s.

[18] However, by observing the TTS S-band ranging signal with a DSN station, a more precise absolute timing measurement of the LGRS clock was achieved. Since the TTS and LGRS use the same clock to time tag measurements, DSN observations of TTS directly correlate LGRS time to UTC. One-way light time from the spacecraft to the DSN station is calculated based on spacecraft orbit position, so the inferred LGRS time tag accuracy depends on spacecraft orbit accuracy. This TTS Direct To Earth (TTS-DTE) measurement could only be made for favorable GRAIL lunar orbit geometries with respect to Earth, which occurs only twice during the Moon's orbit around the Earth. Furthermore, dedicated hardware was needed to track the TTS-DTE signal, which limited TTS-DTE measurements to station DSS-24. The accuracy of the TTS-DTE absolute timing measurement was found to be $\sim 10^{-8}$ s. In addition, the TTS-DTE measurements were used to calibrate the absolute timing measurements from spacecraft time correlation packets [*Kruizinga et al.*, 2013]. The overall GRAIL absolute timing system accuracy was found to be 10^{-6} s.

[19] The USO frequency measurements are based on the one-way RSB Doppler measurement biases estimated every orbit during the orbit determination process. In this process, Doppler corrections are applied for Earth's atmosphere and ionosphere and general relativity. After applying these

Table 1. Summary of the Tracking DATA Used in the GRAIL Primary Mission[a]

	1 March 2012 16:28:00	3 April 2012 13:24:00	3 May 2012 01:09:00	
From/To Arc Length	3 April 2012 13:13:00 (32.71 days)	3 May 2012 00:58:00 (29.44 days)	29 May 2012 16:36:00 (26.55 days)	Total
KBRR	562336	504456	457809	1524601
Two-way S-band Doppler	182902	134050	117801	434753
One-way X-band Doppler	237619	182084	226331	646034

[a]The spacecraft measurements are separated into three intervals with about one month of data each. The first (~March) and third (~May) months contain all the data arcs where part of the spacecraft orbit is in shadow. The spacecraft is in continuous full Sun from 12:20, 2 April 2012 to 18:41, 3 May 2012.

corrections and making a least-squares adjustment of the spacecraft orbit, the residual one-way Doppler bias is related to the USO frequency, since the USO is used to generate RSB X-band carrier, which relates in turn to Ka-band frequency.

[20] Each GRAIL satellite transmits continuous Ka-band microwave carrier-only signals to the other satellite and also receives that satellite's continuous signals. Subtraction of the received signal from the reference signal at each measurement epoch generates a phase measurement. Since both satellites' phase measurements contain nearly identical oscillator drift noises, adding the two phase measurements effectively eliminates the effect of oscillator instability on the range measurement, provided the LGRS clocks have been aligned. After aligning the LGRS clocks and finding the precise LGRS Ka carrier frequency, determined by the USO frequency measurements, the dual one-way phase measurements (integrated frequency) is formed at a given coordinate time t as [*Kruizinga et al*., 2012; *Kim* 2000]

$$\Theta(t) = \varphi_1^2(t) + \varphi_2^1(t) \tag{1}$$

where $\varphi_i^j(t)$ is the differential phase measurement at spacecraft i (determined from the beat frequency of the incoming signal from the other spacecraft and the onboard reference USO), and t is the coordinate time. The differential phase measurement is the difference of the outgoing Ka-carrier phase and the incoming Ka-carrier phase and can be expressed as

$$\varphi_i^j(t) = \varphi_i(t) - \varphi^j(t) + N_i^j + d_i^j + \epsilon_i^j \tag{2}$$

where
$\varphi_i(t)$ = spacecraft i reference phase
$\varphi^j(t)$ = received phase transmitted by spacecraft j
N_i^j = phase ambiguity
d_i^j = phase shift due to instrument, Ka frequency offset, multipath, etc.
ϵ_i^j = random measurement noise

[21] The observed dual one-way range (DOWR) in coordinate time t, or barycentric dynamical time (TDB), is

$$\rho_{\mathrm{DOWR}}(t) = c\frac{\Theta(t)}{f_1 + f_2} \tag{3}$$

where f_1, f_2 are the Ka-band carrier frequencies determined from RSB tracking and c is the speed of light. The lunar gravity determination process requires the transformation of DOWR measurements into Euclidean instantaneous intersatellite range measurements between each spacecraft center of mass (COM). The Euclidean instantaneous intersatellite range is computed according to

$$\rho(t) = \rho_{\mathrm{DOWR}}(t) + \rho_{\mathrm{TOF}}(t) + \rho_{\mathrm{GEOM}}(t) + K \tag{4}$$

[22] The time-of-flight correction, $\rho_{\mathrm{TOF}}(t)$, is the difference between instantaneous Euclidean distance and the computed DOWR (defined below), which accounts for light travel time with relativistic effects. The geometric range correction, $\rho_{\mathrm{GEOM}}(t)$, depends on the spacecraft attitude and accounts for the fact that the Ka phase-center is not located at the spacecraft COM. The constant K represents an ambiguity in the phase measurements that formed the DOWR measurement.

[23] The time-of-flight (TOF) correction is computed with the JPL orbit determination software MIRAGE (Multiple Interferometric Ranging and GPS Ensemble). The two Ka-band signal travel paths, also known as geodesic paths, are then added the same way as the Ka-band phase measurements to form a computed DOWR as

$$\rho_{\mathrm{CDOWR}}(t) = c\frac{f_1\tau_2^1 + f_2\tau_1^2}{f_1 + f_2} \tag{5}$$

[24] The desired one-way light time τ_2^1 and τ_1^2 at reception time t is calculated as well in MIRAGE. The TOF correction is then computed according to

$$\rho_{\mathrm{TOF}}(t) = \rho(t) - \rho_{\mathrm{CDOWR}}(t) \tag{6}$$

[25] It should be noted that the TOF correction accuracy depends strongly on the relative spacecraft orbit accuracy and also depends on the absolute orbit accuracy in the solar system barycentric system.

[26] The objective of the GRAIL science measurement is to observe the relative motion of the COMs of the twin spacecraft. However, the actual measurement is made from the Ka phase center to Ka phase center. The vector from the COM to the Ka phase center is called the Ka boresight vector. Before the geometric range correction can be calculated, the line-of-sight (LOS) vector is calculated from the spacecraft positions according to

$$\mathbf{LOS} = \boldsymbol{r}_1 - \boldsymbol{r}_2$$

where $\boldsymbol{r}_1$ and $\boldsymbol{r}_2$ are the GRAIL position vectors. The geometric range correction is then computed as the projection of the Ka boresight vector on the **LOS** vector.

[27] The phase-derived biased range, ρ_{DOWR}, is converted into instantaneous biased range during preprocessing, with the time-of-flight and geometric corrections applied. Then the instantaneous range-rate (KBRR) and range-acceleration measurements are generated by numerical differentiation of the Euclidean instantaneous range measurement.

[28] The mathematical model of instantaneous range, range rate, and range acceleration observables is summarized in *Kim* [2000] and implemented in the JPL MIRAGE software as follows. The Euclidean distance, or instantaneous range observable, between the two spacecraft can be computed as

$$\rho = \sqrt{(\boldsymbol{r}_1 - \boldsymbol{r}_2)\bullet(\boldsymbol{r}_1 - \boldsymbol{r}_2)} \tag{7}$$

where $\boldsymbol{r}_1$ and $\boldsymbol{r}_2$ are the position vectors of spacecraft 1 and 2, respectively, at a time t. The intersatellite range vector $\boldsymbol{r}_{12}$ and the LOS unit vector, $\hat{\boldsymbol{e}}_{12}$, are defined by

$$\boldsymbol{r}_{12} = \boldsymbol{r}_1 - \boldsymbol{r}_2 = \boldsymbol{LOS}$$
$$\hat{\boldsymbol{e}}_{12} = \boldsymbol{r}_{12}/\rho$$

[29] The range-rate observable is simply obtained by differentiation of the range observable (7) as

$$\dot{\rho} = \dot{\boldsymbol{r}}_{12}\bullet\hat{\boldsymbol{e}}_{12} \tag{8}$$

which represents a projection of the relative velocity vector, $\dot{r}_{12}$, along the LOS unit vector. The range-acceleration

observable can be obtained by differentiation of the range-rate observable (8) to give

$$\ddot{\rho} = \ddot{\boldsymbol{r}}_{12} \bullet \hat{\boldsymbol{e}}_{12} + \dot{\boldsymbol{r}}_{12} \bullet \dot{\hat{\boldsymbol{e}}}_{12} \tag{9}$$

[30] The first term is the projection of the relative acceleration vector, $\ddot{\boldsymbol{r}}_{12}$, along the LOS vector, and the second term is the scalar product of the relative velocity vector and the rate of the LOS vector change. The rate of the LOS vector change can be represented by

$$\rho \dot{\hat{\boldsymbol{e}}}_{12} = \dot{\boldsymbol{r}}_{12} - \dot{\rho} \hat{\boldsymbol{e}}_{12}$$

which denotes the relative velocity component that is perpendicular to the LOS vector.

[31] The instantaneous range-rate (KBRR) and DSN Doppler tracking are the primary data processed by MIRAGE to estimate the satellite states and gravity coefficients. The KBRR data set, derived from LGRS one-way phase measurements, is the main product from the GRAIL Level-1 process [*Harvey et al*., 2012]. This preprocessing of the gravity science data includes analysis of relative timing, absolute timing, USO frequency determination, LGRS clock conversion to TDB coordinate time, Ka boresight vector calibration, and time-of-flight correction for DOWR, and requires precision orbit determination for each GRAIL spacecraft [*Kruizinga et al*., 2013]. In addition to the error contributions in the formulation of the DOWR and KBRR measurement, such as spacecraft orbit and LGRS clock errors, there are other errors within the KBRR observable. These include the thermal expansion of the spacecraft (affecting the boresight vector) and temperature variations of the electronic radio frequency components, including the Ka-band antenna horn that affect the transmitted and measured phase.

4. Gravity Estimation Technique

[32] The lunar gravity field is determined using the same basic technique as previous gravity investigations, for example, used for the Moon [*Konopliv et al*., 2001], Mars [*Konopliv et al*., 2011], and Venus [*Konopliv et al*., 1999] from DSN tracking, and the procedure is similar to the GRACE gravity studies for the Earth [*Tapley et al*., 2004a], except the current study solves for a significantly higher harmonic gravity field. For this study, the computational requirements of the spherical harmonic degree $n = 660$ solution with nearly 437,000 gravity parameters ($\sim n^2$) is about 400 times ($\propto n^4$) more than the previous degree 150 solutions. As a result, supercomputer resources were required, which included the NASA Ames Pleiades, University of Texas Lonestar, and a local JPL gravity cluster with about 800 cores.

[33] The GRAIL spacecraft observations were processed using the JPL software MIRAGE; which is a specialized high precision version of the JPL Orbit Determination Program [*Moyer*, 1971, 2003] developed for the TOPEX mission. MIRAGE was used to process tracking data for all previous JPL planetary gravity studies and the Earth GRACE mission results with its similar interspacecraft measurement system. The complementary GRAIL gravity investigation at GSFC [*Lemoine et al*., 2013] uses the completely independent GEODYN software set.

[34] The three major parts to the gravity estimation process are numerical integration of the spacecraft orbit and partial derivatives of estimated parameters, the determination of the observation equations for the spacecraft DSN tracking data and Ka-band interspacecraft data, and filter processing of the observation equations, where the latter requires the majority of the computational time. MIRAGE numerically integrates the equations of motion in the Moon centered nonrotating coordinate system defined by the inertial International Celestial Reference Frame (ICRF), which is nearly equivalent to the Earth's mean equator at the epoch of J2000. The integrator is a variable order Adams method described in *Krogh* [1973] that adjusts the integration step size to satisfy specified integration tolerances for each parameter being estimated. The number of second-order differential equations to integrate is 3 for spacecraft position, 18 for the position and velocity state transition matrix, and $3N$ where N is the number of nonstate parameter partials to estimate (mostly gravity harmonic coefficients). The integration time is mostly but not completely linear with the number of nonstate (mostly gravity) parameters N (where $N \approx n^2$ and n is the harmonic degree), since reduced integration step size is required as the resolution of the gravity field increases.

[35] For the GRAIL processing, the equations of motion for the spacecraft position $\boldsymbol{r}$ are given by

$$\ddot{\boldsymbol{r}} = \nabla U + \boldsymbol{a}_{\text{pm}} + \boldsymbol{a}_{\text{indirect}} + \boldsymbol{a}_{\text{rel}} + \boldsymbol{a}_{\text{srp}} + \boldsymbol{a}_{\text{alb}} + \boldsymbol{a}_{\text{ir}} + \boldsymbol{a}_{\text{thermal}} + \boldsymbol{a}_{\text{empirical}} \tag{10}$$

where ∇U is the gradient of the lunar gravitational potential, and the remaining terms are the acceleration due to point masses of the planets and Sun, the indirect acceleration in the solar system barycentric frame due to the point masses and oblateness of the Earth, general relativity corrections, the solar radiation pressure force, the acceleration due to lunar albedo and infrared emission, spacecraft thermal reradiation, and empirical constant and once per orbit periodic accelerations to account for any nongravitational mismodeling. The integration of the linearized variational equations [*Tapley et al*., 2004b; *Asmar et al*., 2013] involves partial derivatives of equation (10) with respect to each parameter being estimated, and represents the variation of the orbit from the nominal position and velocity caused by a change in the respective parameter (e.g., a gravity coefficient).

[36] The DSN Doppler and interspacecraft Ka-band range-rate observations are then processed as discussed above and the linearized observation equations are formed. Following the nomenclature of *Tapley et al*. [2004b], the observation residual y is given by the difference of the actual observable Y and computed observable using the nominal orbit $Y^*(t)$ as given by

$$y = Y - Y^*(t) \tag{11}$$

[37] Using the integrated state transition matrix $\Phi(t,t_0)$ to map to the epoch time, the linearized observation equation is then written as

$$y = \left(\frac{\partial G}{\partial X}\right)^* \Phi(t, t_0) x_0 + \epsilon = H x_0 + \epsilon \tag{12}$$

where X are the parameters being estimated and $Y^* = G(X^*)$ is the equation for the observations. The observation error ϵ in equation (12) is then minimized using the vector of residuals y and partials matrix H to determine the corrections x_0 to the nominal epoch values of the estimated parameters.

Table 2. Times of the Maneuvers (AMDs) to Despin the Reaction Wheels Used for Attitude Control[a]

1 March 2012 16:28:00	3 April 2012 13:24:00	3 May 2012 01:09:00
3 April 2012 13:13:00 (32.71 days)	3 May 2012 00:58:00 (29.44 days)	29 May 2012 16:36:00 (26.55 days)
01-MAR-2012 16:16:08	03-APR-2012 13:23:08	03-MAY-2012 01:08:58
01-MAR-2012 16:15:48	03-APR-2012 13:13:07	03-MAY-2012 00:58:53
02-MAR-2012 15:16:38	06-APR-2012 13:18:15	05-MAY-2012 19:23:40
02-MAR-2012 15:06:32	06-APR-2012 13:08:15	05-MAY-2012 19:13:36
06-MAR-2012 22:10:18	12-APR-2012 07:27:47	08-MAY-2012 21:12:11
06-MAR-2012 23:40:06	12-APR-2012 07:17:43	08-MAY-2012 21:02:03
07-MAR-2012 21:45:38	22-APR-2012 02:07:36	11-MAY-2012 17:19:23
07-MAR-2012 21:35:39	22-APR-2012 01:57:33	11-MAY-2012 17:09:16
10-MAR-2012 14:05:48	24-APR-2012 07:06:16	14-MAY-2012 13:26:42
10-MAR-2012 13:55:41	24-APR-2012 06:56:14	14-MAY-2012 13:16:36
13-MAR-2012 15:54:24	26-APR-2012 13:58:55	17-MAY-2012 07:40:53
13-MAR-2012 15:44:19	26-APR-2012 13:48:50	17-MAY-2012 07:30:46
16-MAR-2012 23:23:18	28-APR-2012 22:44:55	19-MAY-2012 22:08:18
16-MAR-2012 23:13:12	28-APR-2012 22:34:54	19-MAY-2012 21:58:12
20-MAR-2012 10:39:03	30-APR-2012 23:56:39	22-MAY-2012 14:29:12
20-MAR-2012 10:28:58	30-APR-2012 23:46:35	22-MAY-2012 14:19:05
23-MAR-2012 21:55:20		25-MAY-2012 04:55:35
23-MAR-2012 21:45:14		25-MAY-2012 04:45:27
27-MAR-2012 19:51:24		27-MAY-2012 19:22:06
27-MAR-2012 19:50:32		27-MAY-2012 19:11:59
28-MAR-2012 02:13:10		29-MAY-2012 16:46:53
28-MAR-2012 02:03:09		29-MAY-2012 16:36:48
30-MAR-2012 07:12:28		
30-MAR-2012 07:02:26		
30-MAR-2012 18:43:30B		
01-APR-2012 12:11:33		
01-APR-2012 12:01:31		

[a]Each time pair represents the midpoint of AMD maneuver time span of GRAIL-A (Ebb) and GRAIL-B (Flow), respectively. Typical maneuver duration is 1–2 min.

[38] The estimate of the gravity field from the observation equations (12) is obtained using a square-root information weighted least squares filter or SRIF [*Lawson and Hanson*, 1995; *Bierman*, 1977]. In normal form, the least-squares solution $\hat{x}$ is given by

$$\hat{x} = \left(H^T W H + P_{\mathrm{ap}}^{-1}\right)^{-1} H^T W y$$

where W is the weight matrix for the observations and P_{ap} is the a priori covariance matrix of the parameters being estimated. In the MIRAGE SRIF filter, the solution equation is kept in the form

$$R\hat{x} = z \tag{13}$$

when processing observations by using Householder transformations. In this equation, R is the upper triangular square-root of the information array or SRIF matrix, and is of fairly large size (760 MB) for a $n = 660$ gravity field. The filter performs the Householder transformations in parallel on the supercomputer using ~1000 CPU cores. This part of the solution process dominates the computer resources ($\propto n^4$), whereas the inversion of R of equation (13) to obtain the gravity solution requires negligible time in comparison (~5 h). The covariance P of the solution (inverse of the information array) is given by

$$P = R^{-1}\left(R^{-1}\right)^T. \tag{14}$$

[39] The tracking data of both spacecraft together are divided into separate time intervals or data arcs of about 2–3 days in length and each arc is processed individually with MIRAGE. The time boundaries of each arc are mostly given by the times of the angular momentum dumps (AMDs) of the reaction wheels (Table 2). As a result, there are no propulsive maneuvers during the data arcs. Otherwise, unmodeled accelerations from the AMDs would corrupt the gravity solution. For each data arc, there are local parameters (e.g., spacecraft position and velocity) that are estimated only for that data arc and global parameters (e.g., gravity coefficients) that are common to all data arcs. First, the solutions for the local parameters of all arcs are iterated to convergence in the Moon centered ICRF system using the nominal gravity field. Second, the SRIF matrices for the local and global parameters are generated for each data arc (a total of 39 matrices for the PM). Third, only the global parameter portions of the SRIF matrices are combined using a similar technique described by *Kaula* [1966] using partitioned normal matrices, and is equivalent to solving for the global parameters plus local parameters of all arcs. The entire solution process is outlined as a flowchart in Figure 2 of *Asmar et al*. [2013].

[40] The local parameters that are estimated include the spacecraft position and velocity, an overall solar pressure scale factor, small corrections to the solar pressure model in the directions orthogonal to the Sun direction, orbit normal and spacecraft along-track constant and periodic empirical accelerations for each orbit with period equal to the orbit period, Ka-band range-rate bias and drift constants, and a time tag offset in the measurement time assigned to the Ka-band data. The global parameters include the Moon's GM, gravitation harmonics to degree 660, and degree-2 and -3 tidal Love number parameters.

Table 3. Nominal Normalized Coefficients ($\times 10^{-10}$) for Dissipation Part of the Lunar Response for Earth and Sun Generated Degree-2 Tides Plus Spin for $k_2/Q = 7\times10^{-4}$ [*Williams*, 2012][a]

Argument α_i	Period (days)	$\Delta\overline{C}_{20i}$	$\Delta\overline{C}_{21i}$	$\Delta\overline{S}_{21i}$	$\Delta\overline{C}_{22i}$	$\Delta\overline{S}_{22i}$
l	27.555	−1.89			3.28	−4.41
F	27.212		4.72	−0.02		
$2D$-l	31.812	−0.36			0.58	−0.88
$2D$	14.765	−0.32			0.75	−0.48
$2l$	13.777	−0.16			0.51	−0.51
$F+l$	13.691		0.64	0.26		

[a]The arguments l, F, D are the Moon's smoothly changing mean anomaly, lunar argument of latitude, and mean elongation of the Moon from the Sun; polynomial expressions are given by *McCarthy and Petit* [2003, p. 48].

5. Spacecraft Force Modeling

[41] The two GRAIL spacecraft are basically proof masses in free fall as they orbit the Moon. All external forces acting on each spacecraft must be precisely modeled such as gravitational forces and nonconservative accelerations as listed in equation (10). The lunar gravitational potential U is modeled by a spherical harmonic expansion in the body-fixed reference frame with normalized coefficients ($\overline{C}_{nm}$, $\overline{S}_{nm}$) and is given by [e.g., *Heiskanen and Moritz*, 1967; *Kaula*, 1966]

$$U = \frac{GM}{r} + \frac{GM}{r}\sum_{n=2}^{\infty}\sum_{m=0}^{n}\left(\frac{R_e}{r}\right)^n \overline{P}_{nm}(\sin\phi) \left[\overline{C}_{nm}\cos(m\lambda) + \overline{S}_{nm}\sin(m\lambda)\right] \quad (15)$$

where GM is the gravitational constant times the mass of the central body, n is the degree, m is the order, $\overline{P}_{nm}$ are the fully normalized associated Legendre polynominals, R_e is the reference radius of the body, $\varphi_{\rm lat}$ is the latitude, and λ is the east longitude. The gravity coefficients are normalized such that the integral of the harmonic squared equals the area of a unit sphere, and are related to the unnormalized coefficients as [*Kaula*, 1966; *Lambeck*, 1988]

$$\begin{pmatrix} C_{nm} \\ S_{nm} \end{pmatrix} = \left[\frac{(n-m)!(2n+1)(2-\delta_{0m})}{(n+m)!}\right]^{1/2}\begin{pmatrix} \overline{C}_{nm} \\ \overline{S}_{nm} \end{pmatrix} = f_{nm}\begin{pmatrix} \overline{C}_{nm} \\ \overline{S}_{nm} \end{pmatrix} \quad (16)$$

[42] The corresponding normalized Legendre polynomials $\overline{P}_{nm}$ are thus related to the unnormalized polynomials P_{nm} by $P_{nm} = \overline{P}_{nm}/f_{nm}$. The degree-1 coefficients are zero since the coordinate system's origin is the center-of-mass, and the longitude independent zonal coefficients $\overline{J}_n$ are given by $\overline{J}_n = -\overline{C}_{n0}$.

[43] The acceleration due to the lunar tide on the GRAIL spacecraft is also modeled as time-varying changes to all degree-2 and -3 gravity coefficients as [*McCarthy and Petit*, 2003, pg. 59]

$$\Delta\overline{C}_{nm} - i\Delta\overline{S}_{nm} = \frac{k_{nm}}{2n+1}\sum_{j=2}^{3}\frac{GM_j}{GM_{\rm Moon}}\left(\frac{R_e}{r_j}\right)^{n+1}\overline{P}_{nm}(\sin\phi_j)e^{-im\lambda_j} \quad (17)$$

where k_{nm} are the frequency-independent lunar Love numbers, j represent the tidal disturbing bodies (Earth and Sun), r_j is the distance from the Moon to the disturbing body, and φ_j is the latitude and λ_j is the longitude of the disturbing body in the lunar body-fixed frame. Only the real or elastic part of k_{nm} is considered in equation (17), and for each degree the Love numbers for different orders are expected to be nearly equal. These coefficient expressions consist of a constant plus periodic part (~monthly). The constant or permanent

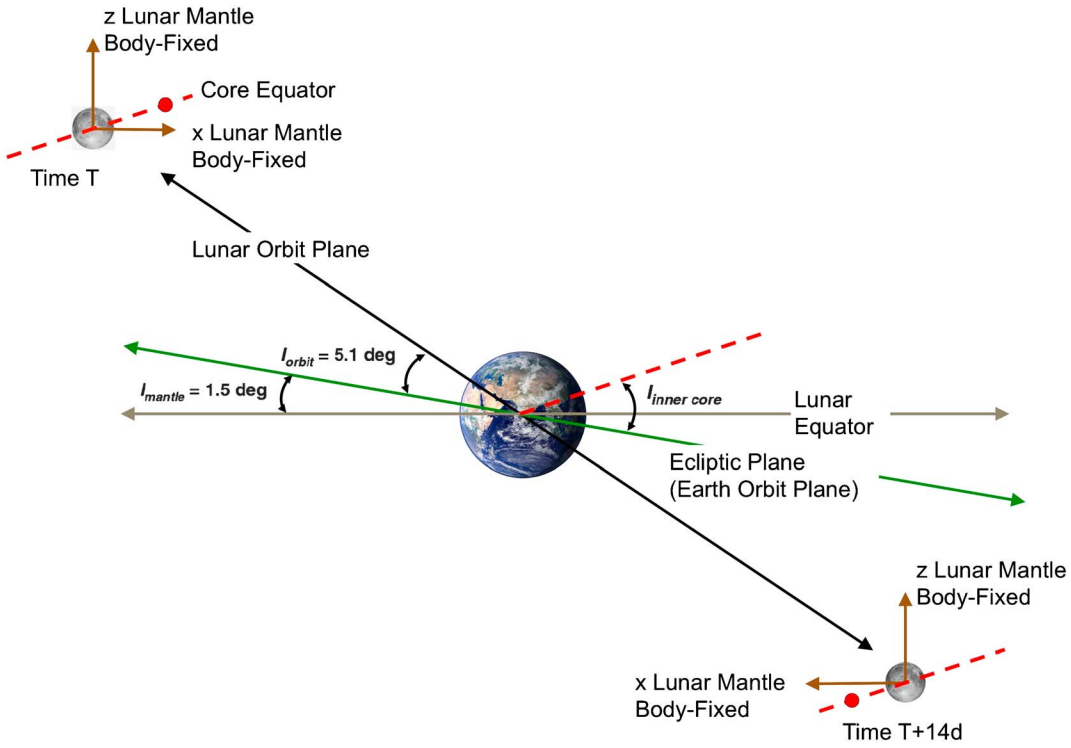

Figure 7. The Motion of the Moon's inner core due to a tilt of the core equator with respect to the body-fixed or mantle frame. Note that a point (red dot) on the x-axis of the core shifts from above the mantle x-axis to below and back with each month.

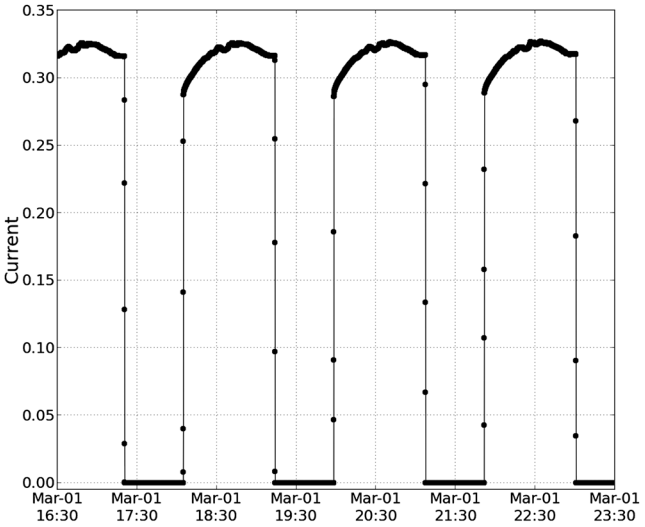

Figure 8. Sample current data from the spacecraft engineering telemetry showing entrance and exit from solar eclipse.

parts of the tide are not included in the corresponding published values of the gravity coefficients for the JPL lunar gravity fields.

[44] The time-varying terms of the degree-2 dissipative part of the tide are modeled as periodic variations in the gravity coefficients [*Williams*, 2012] that are in addition to the elastic tide in (17). However, since specific dissipation $Q \approx 37$ [*Williams et al.*, 2013] the largest dissipative terms are about 3% of the size of the elastic tide of (17). The six largest periodic dissipative terms for the degree-two coefficients are given by

$$\begin{aligned}
\Delta\overline{C}_{20} &= \sum_{i=1}^{6} \Delta\overline{C}_{20i}\sin(\alpha_i) \\
\Delta\overline{C}_{21} &= \sum_{i=1}^{6} \Delta\overline{C}_{21i}\cos(\alpha_i) \\
\Delta\overline{S}_{21} &= \sum_{i=1}^{6} \Delta\overline{S}_{21i}\sin(\alpha_i) \\
\Delta\overline{C}_{22} &= \sum_{i=1}^{6} \Delta\overline{C}_{22i}\sin(\alpha_i) \\
\Delta\overline{S}_{22} &= \sum_{i=1}^{6} \Delta\overline{S}_{22i}\cos(\alpha_i)
\end{aligned} \tag{18}$$

where the amplitudes and arguments are given in Table 3.

[45] There is another possible periodic time-varying signature due to the Moon's inner solid core that might be as large as the dissipative tide, although a search for this signature will be addressed in future studies with the combined GRAIL primary and extended mission data. The Moon possibly has a solid inner core and a fluid outer core [*Weber et al.*, 2011]. Given a triaxial inner core and a tilt of the inner core equator relative to the mantle equator, a time-varying monthly signature [*Williams*, 2007] can result from the relative motion of the inner core axes relative to the lunar body-fixed or mantle-fixed frame as shown by Figure 7. Since GRAIL observes the combined gravity of the mantle and core, the relative motion of between the two solid structures gives rise to a monthly periodic C_{21} and S_{21} signature. Both mantle and inner core equators are inclined with respect to the ecliptic plane. The mantle inclination $I_m = 1.543°$ is directly measured by LLR while the inner core inclination I_{ic} is unknown. Assuming a small inclination difference $I_m - I_{ic}$ between the inner core and mantle equators gives the periodic signature [*Williams*, 2007]

$$\begin{aligned}
\Delta C_{21} &= -\sin(I_m - I_{ic})\{J_{2_{ic}}\sin F + 2C_{22_{ic}}\sin(F + 2\tau_{ic})\} \\
\Delta S_{21} &= -\sin(I_m - I_{ic})\{J_{2_{ic}}\cos F - 2C_{22_{ic}}\sin(F + 2\tau_{ic})\}
\end{aligned} \tag{19}$$

where J_{2ic} and C_{22ic} are the inner core unnormalized J_2 and C_{22} gravity coefficients for the inner core principal axes scaled to the whole Moon mass and radius. The angle of the inner core equatorial principal axes relative to the mantle equatorial axes is given by τ_{ic}, and F is the same lunar argument of latitude as in the dissipative tidal terms.

[46] The gravity harmonics and tidal expressions are given in the lunar body-fixed coordinate system defined by the principal axes of the integrated lunar physical librations from JPL planetary ephemeris DE421 [*Williams et al.*, 2008]. The three Euler angles (about z, x, and z) on DE421 describe the rotations from the ICRF x-axis to the intersection of the lunar equator with the ICRF equator, the obliquity of the lunar equator with respect to ICRF equator, and the rotation to the principal body-fixed prime meridian or x-axis. In this principal axis frame, we expect solutions for the degree-2 coefficients C_{21}, S_{21}, and S_{22} to be nearly zero as a result. The principal axes from the integrated librations differ from the axes of the mean-pole system of the IAU [*Archinal et al.*, 2011] by ~100″ and the IAU periodic representation of the librations is an approximation that differs from the integrated librations by ~100 m on the surface of the Moon [*Konopliv et al.*, 2001].

[47] Unlike the GRACE mission, which has an accelerometer to measure the effects of the Earth's atmosphere (along with solar and Earth-reflected radiation pressure, and any spacecraft thermal emission), the GRAIL mission must accurately model or estimate from the data all nongravitational accelerations to determine the lunar gravity field. The spacecraft accelerations to consider in decreasing order of importance are the solar radiation pressure, the spacecraft thermal emission, the lunar albedo refection from the Moon's surface, and the thermal infrared emission from the Moon's surface.

[48] The solar radiation pressure acceleration is the largest nongravitational acceleration near at most 1×10^{-10} km/s^2 [*Park et al.*, 2012]. The spacecraft bus (1.58, 0.76, 0.62 m^2 area for each face normal to the x, y, and z-axis, respectively) and solar arrays (3.86 m^2 total area) are modeled as three and one flat plates, respectively, with expected specular and diffuse reflectivity coefficients [*Fahnestock et al.*, 2012]. The estimation of an overall scale factor times the solar pressure acceleration removes the majority of any mismodeling due to incorrect reflectivity coefficients, with relatively little degradation of the gravity solution through correlation with these parameters. In addition, two small solar pressure coefficients normal to the Sun direction account for mismodeling in those directions of less than 1% of the overall force.

[49] The potentially largest error of the solar pressure model is the timed entrance and exit of the GRAIL spacecraft into solar eclipse (i.e., lunar shadow as given by the partially lit penumbra and dark umbra). The shadow crossing times and the fraction of solar output on the solar arrays during partial shadowing (penumbra) are given by the solar array current output from the spacecraft telemetry for one solar cell (see Figure 8). Due to the heating of the solar array as it enters

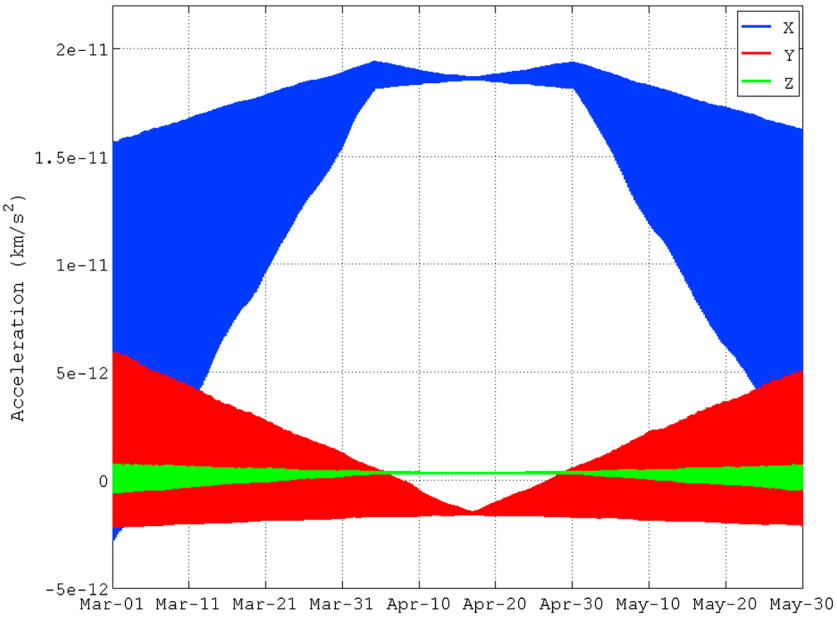

Figure 9. Model derived acceleration on GRAIL-A (Ebb) due to the spacecraft thermal emission over the duration of the PM. The spacecraft *X*, *Y*, and *Z* axes represent the spacecraft orbit normal (or solar array normal), radial, and along-track (or near the spacecraft velocity) directions.

the sunlight, the current output does not reach an instantaneous maximum. For this reason, we designate any current within 20% of the maximum as full Sun. The entrance and exit into solar eclipse as given by telemetry appears to be accurate to ~2–3 s.

[50] The next largest nongravitational acceleration is that due to the infrared radiation of heat from the spacecraft (about 5× smaller than the solar pressure acceleration). Currently, the accelerations from this model are not included in the force model for the GRAIL processing, but will be in future

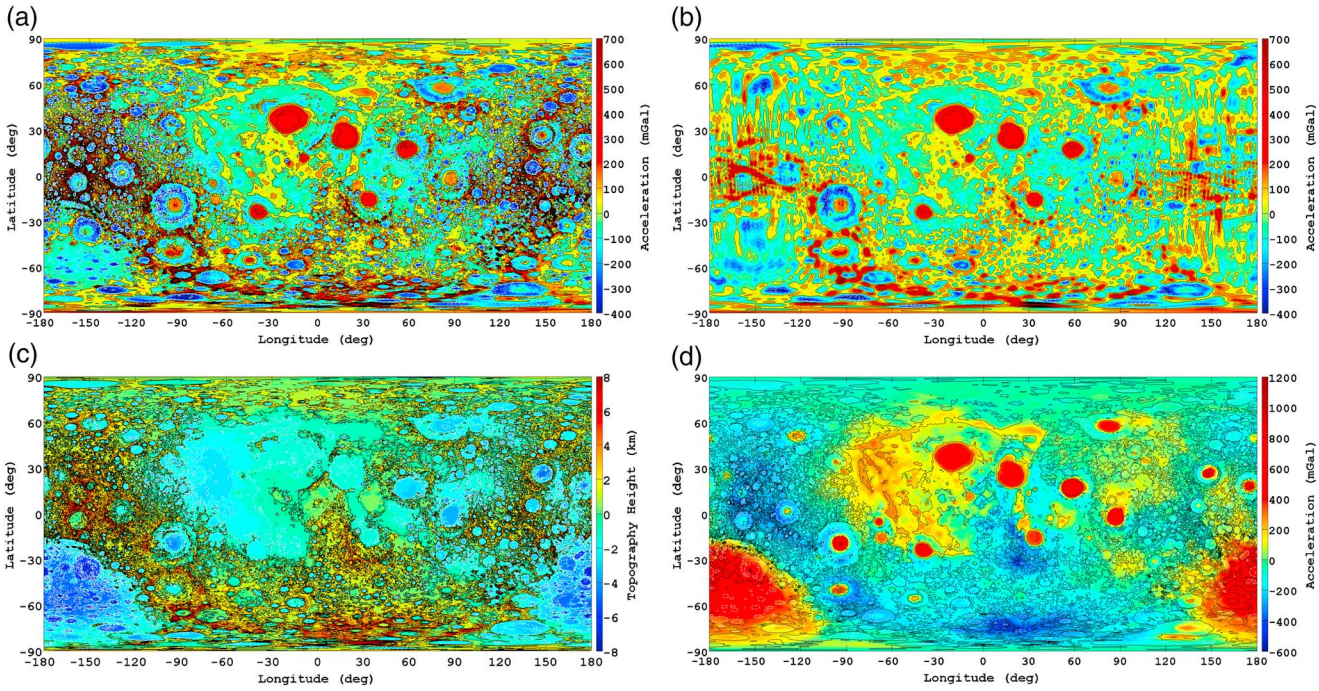

Figure 10. Global maps of the Moon for (a) the surface radial acceleration of the GRAIL lunar gravity field GL0660B truncated at degree 360 (max = 1268 mGals, min = −645 mGals, positive downward), (b) the older Lunar Prospector LP150Q gravity field through degree 140, (c) the LRO surface topography [*Smith et al.*, 2010], and for (d) Bouguer acceleration or gravity minus gravity from topography truncated at degree 330 (max = 1152 mGals, min = −644 mGals). Accelerations are shown on the lunar reference sphere of 1738 km.

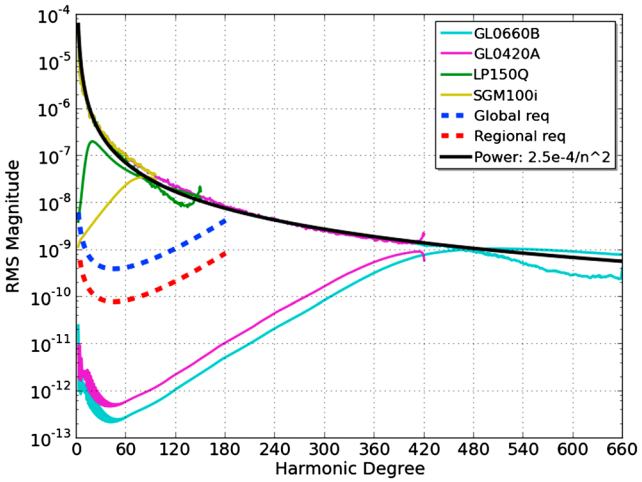

Figure 11. The RMS magnitude gravity spectrum for the GRAIL gravity fields GL0420A [*Zuber et al.*, 2013b], GL0660B (this paper), the Lunar Prospector gravity field LP150Q [*Konopliv et al.*, 2001], and the SELENE SGM100i model [*Goossens et al.*, 2011]. GRAIL far exceeded the global and regional science requirements for the mission [*Zuber et al.*, 2013a].

efforts to detect the core periodic signature and improve the low-degree harmonics of the gravity field. However, the expected sizes of the periodic variations of the modeled thermal reradiation acceleration are used to set the a priori amplitudes of the estimated empirical accelerations. These periodic amplitudes together with the solar pressure scale factor remove most of the error expected from the thermal reradiation acceleration model. The thermal reradiation acceleration model is derived from 28 flat-plate surfaces of GRAIL assuming black-body radiation for each plate surface [*Fahnestock et al.*, 2012] that uses the spatially averaged temperature, varying as a function of time, for each surface. The spacecraft average surface temperature profiles for different solar beta angles were computed using detailed thermal finite element modeling at Lockheed Martin, which built the GRAIL spacecraft.

[51] Figure 9 shows the predicted acceleration of the spacecraft thermal model for the Primary Mission. The thermal emission acceleration is nearly constant during the full Sun or middle month of the PM and has large periodic variations within each orbit for the smaller solar beta angles. The constant part of the acceleration will be absorbed in the solar pressure scale factor estimate, so we need only to absorb any mismodeling of the periodic part of the thermal model with the periodic empirical acceleration model. The periodic part is largest when the solar eclipse is the longest (greatest temperature variation) and is mostly given by a once per orbit signature. The periodic component in the orbit plane normal direction is the largest because the emission from the spacecraft solar arrays dominates the force, and peaks at about 1.5×10^{-11} km/s^2 at the beginning and end of the PM. The smallest amplitude assumed for the full Sun period is 3×10^{-13} km/s^2. Such periodic empirical accelerations are estimated only in the orbit normal and spacecraft along-track directions. The radial component is not estimated to avoid absorbing gravity signature.

[52] After the spacecraft thermal emission model, the next largest source of error for the spacecraft accelerations is due to the lunar albedo reflection and lunar thermal radiation incident on the spacecraft. These are fairly small accelerations ($\sim1\times10^{-12}$ km/s^2) that are 10 times smaller than the spacecraft thermal emission acceleration and 50 times smaller than the solar radiation pressure acceleration. The acceleration due to lunar-reflected sunlight is computed using the Delft Lunar Albedo Model 1 derived from Clementine imagery [*Floberhagen et al.*, 1999], a 10th degree and order spherical harmonic representation of the lunar albedo. The simple lunar thermal emission model [*Park et al.*, 2012] is assumed proportional to $T^4 \cos\psi_s$ where T is the maximum lunar surface temperature ($T = 382.86$ K) and ψ_s is the lunar centered angle between the surface location and Sun direction. Comparisons with the Lunar Reconnaissance Orbiter's (LRO) Diviner Lunar Radiometer Experiment indicate at most a 10% error in the accelerations (i.e., $\sim10^{-13}$ km/s^2).

6. Gravity Solution

[53] The spherical harmonic gravity solution to degree and order 660 (named GL0660B for GRAIL Lunar) is an update of the preliminary field (GL0420A in *Zuber et al.* [2013b]). Both solutions are based upon the 3 months of DSN and Ka-band range rate data during the GRAIL Primary Mission. The addition of higher-degree harmonics allows for extended resolution in regions supported by the data and removes aliasing effects in the higher degrees (~360 to 420) of the previous solution GL0420A. Mapped to the lunar reference sphere (Figure 10), GL0660B shows unprecedented detail of the gravity field both on the lunar nearside and farside.

[54] The lunar gravity RMS spectrum in Figure 11 as given by

$$M_n = \sqrt{\frac{\bar{C}_{nm}^2 + \bar{S}_{nm}^2}{2n+1}} \tag{20}$$

displays the overall average global resolution to be near degree 420 (13 km half-wavelength surface resolution), the degree where the uncertainty in the spectrum is equal to the expected power. The improvement in the gravity field from LP without direct farside observation to direct observation with SELENE

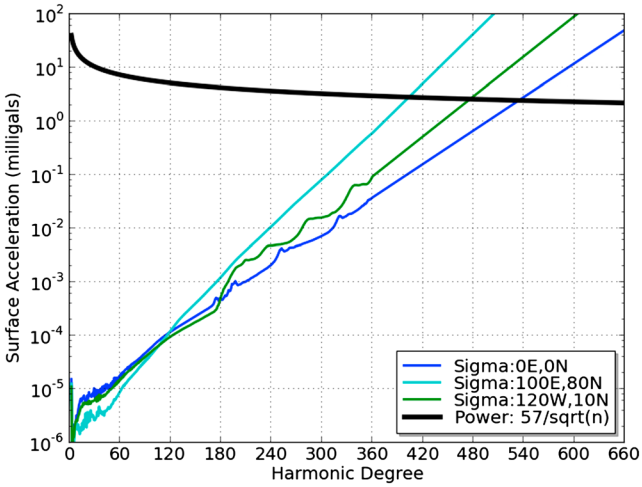

Figure 12. The surface acceleration error for three locations on the lunar surface corresponding to higher altitude (100°E, 80°N) and lower altitude (0°E, 0°N and 240°E, 10° N; see Figure 6). The expected signal of the acceleration per harmonic degree is also displayed.

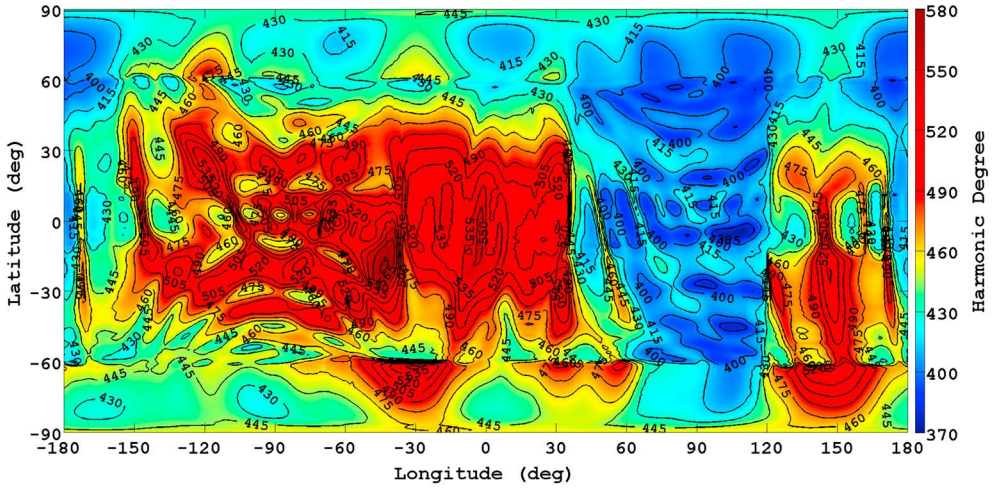

Figure 13. The resolution of the GL0660B gravity field in harmonic degree as a function of latitude and longitude.

is evident. The 4 orders-of-magnitude improvement in the GRAIL velocity measurement (KBRR) versus previous missions (DSN S-band Doppler) translates directly into 4 or more than 5 orders-of-magnitude improvement for the vast majority of the gravity spectrum as shown in Figure 11. The GRAIL gravity solutions from the primary mission also far exceeded the science global and regional requirements for the mission [*Zuber et al*., 2013a] as noted by the blue and red dashed lines, respectively. The tightened KBRR weighting of this solution from 0.1 μm/s to the more appropriate 0.03 μm/s is the cause of the improvement in the gravity uncertainty spectrums from the GL0420A to GL0660B solutions. The spectrum of the gravity coefficients approximately follows the $0.00025/n^2$ power law [*Kaula*, 1966], which was used for the LP150Q model. A fit of the harmonics from degree 150 to degree 440 gives the slightly different power law $0.0010973/n^{2.2659}$.

[55] Since the solution is determined for a degree 660 that is beyond the global resolution of the data, a power law constraint is applied to the higher degrees to smooth the solution and limit noise. The constraint begins at harmonic degree 331 and biases the coefficients toward zero with an uncertainty equal to the more relaxed power law $0.00036/n^2$. The result of the relaxed constraint is evident in Figure 11 where the GL0660B uncertainty curve is greater than the power law for the higher degrees.

[56] The variable resolution of the gravity field over the surface can be characterized using the covariance matrix from the GL0660B solution using the same technique of *Konopliv et al*. [1999]. The RMS acceleration at the lunar surface for all coefficients of degree n is given by

$$(a_n)_{\mathrm{RMS}} = \frac{GM}{R_e^2} K \sqrt{2/n} \tag{21}$$

where K is the Kaula constant of 0.00025 from the power law. For the Moon, the global average surface acceleration reduces to

$$(a_n)_{\mathrm{RMS}} = 57/\sqrt{n} \ \text{mGals}. \tag{22}$$

[57] This is the expected signal profile of the acceleration for all points on the lunar surface assuming the gravity coefficients follow the $1/n^2$ power law. The uncertainty in the surface acceleration for harmonic degrees from 2 to n, $\sigma(a_{2,n})$, can also be determined from the covariance matrix as a function of latitude and longitude, and is given by

$$\sigma(a_{2,n})^2 = \left(\frac{\partial a_{2,n}}{\partial \vec{g}_{2,n}}\right)^T P_{2,n} \left(\frac{\partial a_{2,n}}{\partial \vec{g}_{2,n}}\right) \tag{23}$$

where $\vec{g}_{2,n}$ is the vector of all normalized gravity coefficients from degree 2 to n and $P_{2,n}$ is the corresponding covariance. The covariance of the coefficients from degree 2 to n is the covariance as if the higher-degree coefficients ($>n$) are not estimated. Hence, it is a truncation, or submatrix, of the full GL660B covariance without any constraint applied to the gravity field. The uncertainty from the coefficients only at degree n is

$$\sigma(a_n) = \sigma(a_{2,n}) - \sigma(a_{2,n-1}). \tag{24}$$

[58] In order to facilitate the computation of the spatial resolution, the covariance matrix from GL0660B is truncated

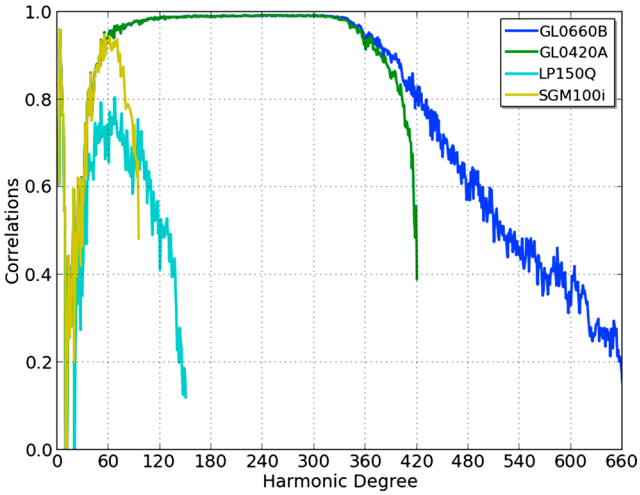

Figure 14. Correlation of the GRAIL and previous gravity solutions with LOLA topography converted to gravitational potential.

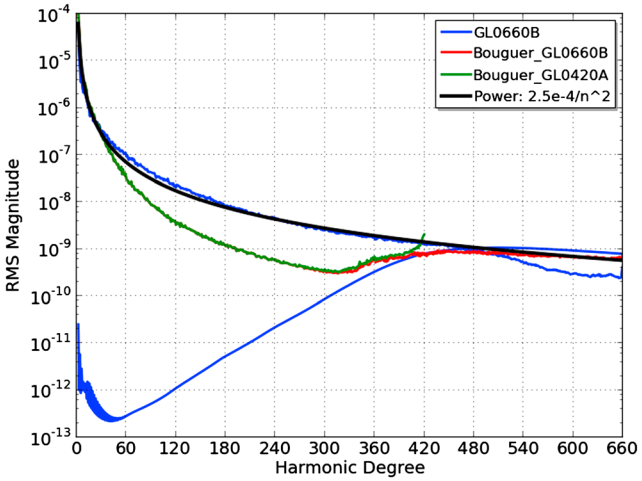

Figure 15. The Bouguer RMS magnitude spectrum showing the difference between the gravity coefficients of GL0420A and GL0660B and the gravitational potential coefficients derived from the LOLA topography.

at degree 360 and the remaining uncertainty in the surface acceleration is extrapolated to higher degrees. Figure 12 shows the surface error profiles for three different points on the surface that represent one higher and two lower altitudes. The harmonic degree at which the acceleration error of equation (24) equals the signal of equation (22) determines the harmonic resolution of the gravity field for that location on the surface. Figure 13 shows this crossing point of each acceleration profile with the power law, or the gravity resolution in harmonic degree for all locations on the surface. The resolution varies over the surface from $n = 371$ to $n = 583$, with the poorest resolutions apparent for the higher altitude regions near 90°E and the higher latitudes. There is an unexplained artifact in the covariance at 30°W-60°S and at a 180° longitude shift (150°E) that may be a result of two low altitude arcs from 4 March and 25 May crossing at the pole. The total uncertainty of all harmonics (i.e., the integrated profile in Figure 12) to the crossing point of the Kaula power curve is fairly uniform over the entire lunar surface and is bounded between 10 and 12 mGals.

[59] The majority of the gravity signal at higher degrees is derived from the surface topography [*Zuber et al.*, 2013b]. The global correlation between the LRO topographic potential, or gravitational potential computed from topography [*Smith et al.*, 2010], to 9th power [e.g., *Wieczorek and Phillips*, 1998] and the GRAIL gravity models exhibit global correlation to better than 98% between harmonic degrees 120 and 330, as shown in Figure 14. The difference of the gravity coefficients from the topographic coefficients or Bouguer anomaly spectrum is shown in Figure 15, and it reveals the Bouguer spectrum is good to degree 330 [*Wieczorek et al.*, 2013]. As a global average, there is only slight improvement in the Bouguer anomaly by extending the solution to harmonic degree 660 from 420. However, there are some regional areas that are significantly extended in Bouguer resolution. From Figure 12, a power law for the Bouguer RMS spectrum that is 10× smaller ($5.7/n^{1/2}$ mGals) than the gravity power law, indicates a crossing of the noise and signal that is biased by about 70–80 degrees for all locations. The resulting Bouguer resolution then takes similar form to Figure 13 with a covariance derived range from $n = 304$ to a best resolution of $n = 480$ for the low-altitude areas near the equatorial region.

[60] The significant improvement of the degree-2 and -3 gravity coefficients from the GRAIL mission in turn improve

Table 4. The Solutions for the Moon's *GM*, Tidal Love Numbers and Degree-2 and -3 Unnormalized Gravity Coefficients Based Upon the Entire GRAIL Primary Mission (PM) Unless Otherwise Noted[a]

Parameter	Solution	Comment
GM	4902.80031 ± 0.00044	Lunar solar system barycentric *GM*
$\overline{J}_2$	9.0880835e-5 ± 1.4e-9	GRAIL PM, normalized without permanent tide
$\overline{C}_{21}$	1.2e-10 ± 1.3e-10	"
$\overline{S}_{21}$	1.01e-9 ± 1.6e-10	"
$\overline{C}_{22}$	3.4673798e-5 ± 1.7e-9	"
$\overline{S}_{22}$	−2.5e-10 ± 2.8e-10	"
$\overline{J}_3$	3.1974673e-6 ± 1.4e-11	"
$\overline{C}_{31}$	2.6368046e-5 ± 1.6e-11	"
$\overline{S}_{31}$	5.4545196e-6 ± 1.4e-11	"
$\overline{C}_{32}$	1.4171529e-5 ± 2.4e-11	"
$\overline{S}_{32}$	4.8779630e-6 ± 2.8e-11	"
$\overline{C}_{33}$	1.2274951e-5 ± 7.2e-11	"
$\overline{S}_{33}$	−1.7743956e-6 ± 6.3e-11	"
J_2	2.0330530e-4	GRAIL PM, unnormalized with permanent tide
C_{22}	2.242615e-5	"
k_2	0.02405 ± 0.00018	GRAIL PM
k_2	0.0248 ± 0.003	LP150Q, *Konopliv et al.* [2001]
k_2	0.0240 ± 0.0015	SGM100h, *Matsumoto et al.* [2010]
k_2	0.0255 ± 0.0015	SGM100i, *Goossens et al.* [2010]
k_2	0.02405 ± 0.00018	GRAIL PM, k_{20}, k_{21}, k_{22} constrained to be equal
k_{20}	0.02408 ± 0.00045	GRAIL PM
k_{21}	0.02414 ± 0.00025	GRAIL PM
k_{22}	0.02394 ± 0.00028	GRAIL PM
k_2	0.02425 ± 0.00024	GRAIL middle month of PM (~April), full Sun
k_3	0.0089 ± 0.0021	GRAIL PM

[a]Multiple degree-2 Love number solutions are presented; k_{20}, k_{21}, and k_{22} contribute to the J_2, order one (C_{21}, S_{21}), and order 2 (C_{22}, S_{22}) gravity coefficients respectively as given by equation (17). All combined k_2 solutions constrain $k_{20} = k_{21} = k_{22}$. Note formal uncertainties are increased by a factor of 40 to obtain realistic errors.

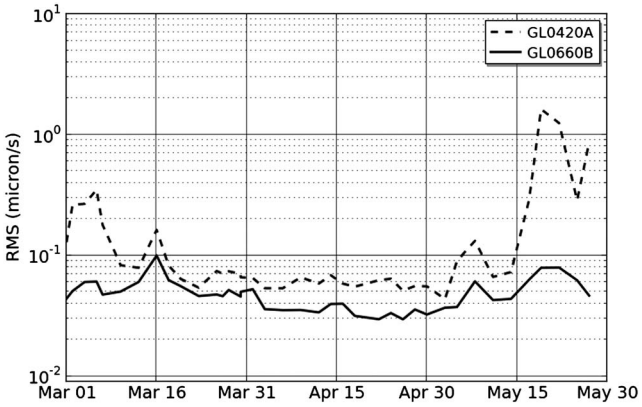

Figure 16. GRAIL KBRR residual RMS for each arc of the Primary Mission. The residuals are shown for the GL0420A solution of *Zuber et al*. [2013a] and GL0660B of this paper.

the processing of the LLR data and the determination of the Moon's moments of inertia (*J. G. Williams et al*., Lunar interior properties from the GRAIL mission, submitted to *Journal of Geophysical Research*, 2013). The new low-degree gravity coefficients also significantly improve the lunar physical librations, which define the body-fixed principal axes of the Moon used for the gravity estimation. Future GRAIL results will include data analysis with a new JPL ephemeris with updated librations, instead of DE421. The solutions for the low-degree coefficients are very sensitive to the libration model used and to the models of the nongravitational acceleration on the GRAIL spacecraft including the empirical periodic acceleration model.

[61] The solutions for the degree-2 and -3 coefficients, Moon's *GM* and degree-2 and -3 Love numbers are given in Table 4. Due to current mismodeling in the spacecraft nongravitational accelerations and lunar physical librations, the formal uncertainties of each parameter from the covariance are scaled by 40 to give a more realistic error. This scaling was obtained by computing RMS differences between gravity solutions with different empirical periodic assumptions (10^{-11} km/s^2 and much tighter), and diminishes

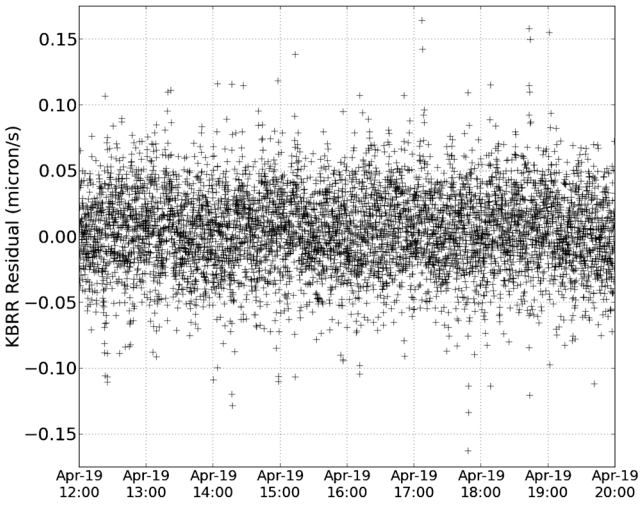

Figure 17. Sample KBRR residual plot for four orbits of one data arc. The KBRR residuals for this data arc have an RMS of 0.03 μm/s (units on the *y*-axis are km/s).

as the harmonic degree increases (~1 for $n > 100$), comparisons between JPL and GSFC solutions (*Williams et al*., submitted manuscript, 2013), and in variations of arc-dependent parameters as noted later. One curious result is a significant nonzero S_{21} gravity coefficient in both the JPL and GSFC solutions that implies a nonprincipal axis frame for the whole Moon (mantle plus core) gravity field despite contrary indications from the LLR physical libration solutions [*Williams et al*., 2013]. The cause is not currently understood. The *GM* solution variations indicate that the *GM* derived from joint planetary ranging and LLR has lower uncertainty than the current GRAIL-derived solutions based upon the Primary Mission.

[62] GRAIL has now determined the Love number to better than 1%, $k_2 = 0.02405 \pm 0.00018$, which is an improvement over previous individual spacecraft uncertainties by ~10× [*Goossens et al*., 2011; *Matsumoto et al*., 2010; *Konopliv et al*., 2001] or ~5× for previously combined results with LLR (*Williams et al*., submitted manuscript, 2013). The uncertainty in the solution for the k_2 Love number is inferred by comparing solutions for each harmonic order k_{2m} (a variation of 0.5%) and with solutions for the middle month of the PM (a difference of 0.8%), which has minimal nongravitational spacecraft errors. The degree-3 Love number is determined to about 25% with the formal errors scaled up by 40. Future improvements in the long-wavelength modeling have the potential to reduce the k_3 solution errors by 10×.

7. Spacecraft Orbit Solutions and Other Parameters

[63] During the GRAIL PM, multiple tests were performed to monitor the progress of the gravity solutions. These tests were repeated as more GRAIL KBRR data were collected and as the degree and order of the gravity solutions increased.

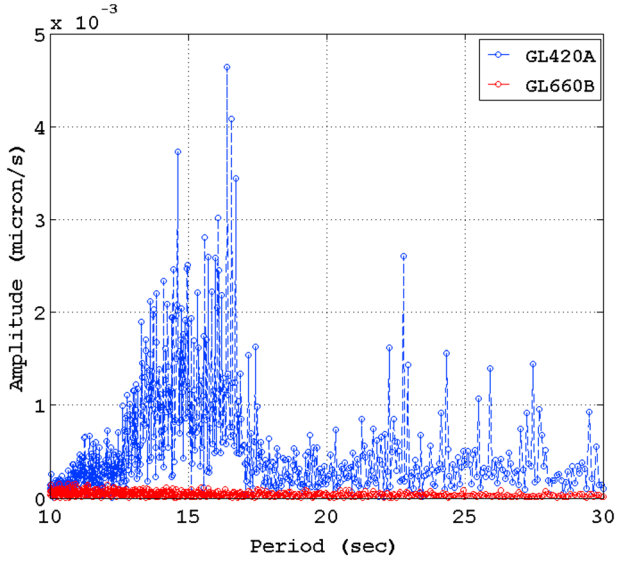

Figure 18. The FFT of the GRAIL KBRR residuals from the entire Primary Mission for the GL0420A and GL0660B gravity fields. The figure represents the high frequency content of the residuals. A 420 degree field has wavelength 26 km, which the spacecraft traverses in 16 s. Thus, a gravity field to $n = 420$ cannot absorb signature with period less than ~16 s.

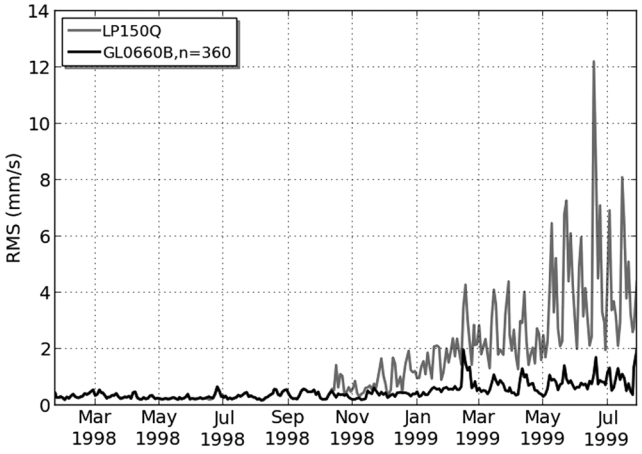

Figure 19. Residual fit RMS of the LP Doppler tracking data for the entire LP nominal mission (1 year at an average 100 km altitude) and extended mission (7 months at 25–35 mean altitude). The orbits were fit using an arc length of 2 days.

In addition to the evaluation of the gravity spectrum and correlation to topography as discussed above, other tests included the total RMS fit of each data arc for the DSN and KBRR residuals, fast Fourier transform (FFT) analysis of the KBRR residuals, GRAIL spacecraft orbit overlap errors, GRAIL KBRR time-tag solutions, LP orbit solutions, and fit of Ka-band instantaneous range (KBR) data during calibration attitude maneuvers.

[64] At the beginning of the PM, the initial fits of the KBRR residuals were very large using the nominal LP150Q field, with residuals between 1–10 mm/s (or almost 10^6 times the data noise). Significantly larger residuals with respect to LP150Q were observed for the lunar farside highlands versus the previously observed nearside. As shown in Figure 16, the fit of the KBRR residuals is very near the data noise when using the current GL0660B field, especially for the central part of the Primary Mission of April 2012 with continuous full Sun on the spacecraft (see Figure 17). The residuals for the lower-altitude data at the beginning of March and end of May depend on the resolution of the field and are ~10× larger for the lower resolution GL0420A field. We also expect the residuals for the months with the spacecraft in solar eclipse to improve as spacecraft shadow crossing and other nongravitational models improve. The FFT of the GL0420A and GL0660B residuals in Figure 18 shows the improvement in the high frequency part of the gravity field.

[65] As the gravity fields using only GRAIL data progressed, the corresponding orbit fits of the LP tracking data, especially of the lower-altitude LP extended mission (30–40-km mean altitude), gave an independent assessment of the gravity field fidelity. Figure 19 shows the RMS fit of the entire LP nominal (~100-km mean altitude) and extended mission using the LP gravity model LP150Q and the GL0660B model truncated at degree $n = 360$. The fits of the

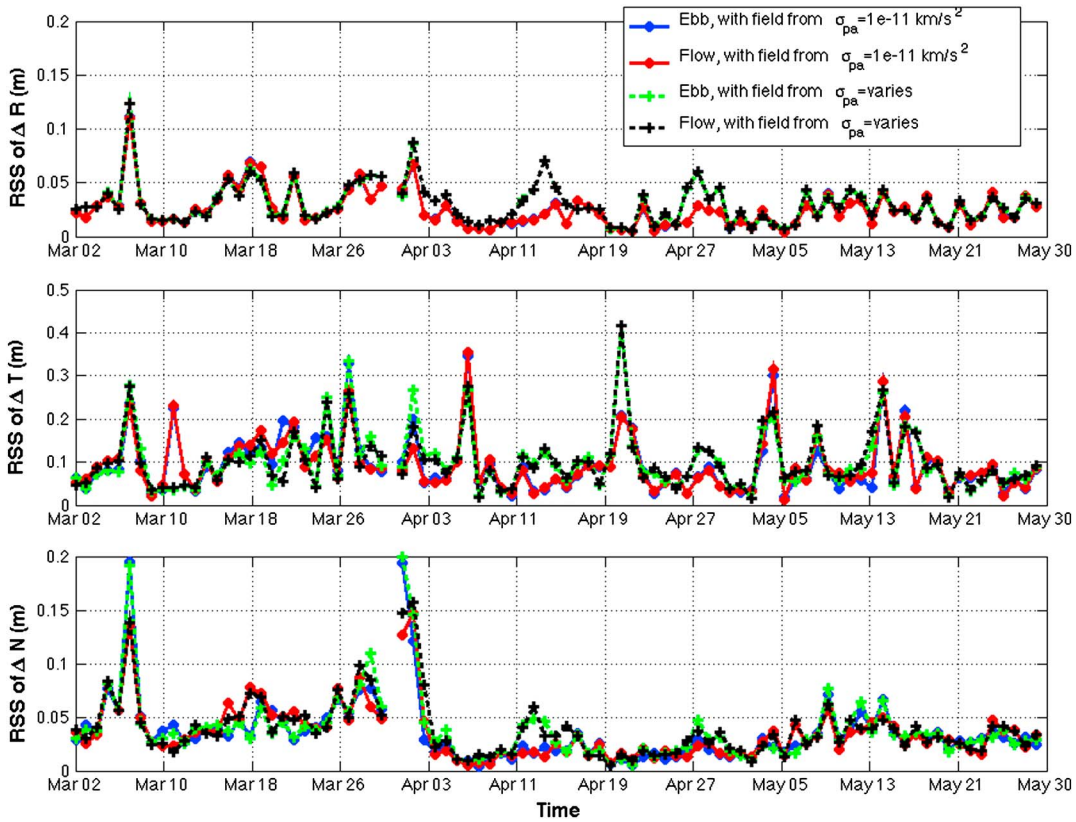

Figure 20. Spacecraft radial (R), along-track (T), and orbit normal (N) overlap errors in meters for GRAIL-A (Ebb) and GRAIL-B (Flow) for the Primary Mission using two similar gravity fields: (1) the GL0660B gravity field where the periodic acceleration model varies versus solar beta angle, and (2) where the gravity field is developed using a uniform a priori 10^{-11} km/s^2 acceleration.

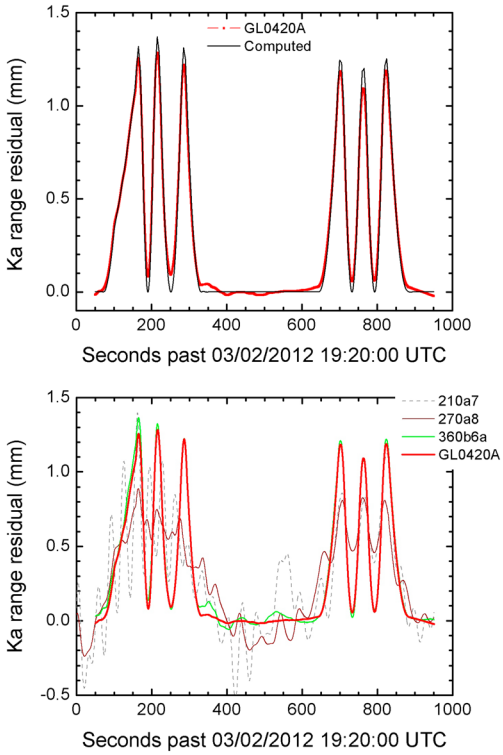

Figure 21. The Ka-band range residuals from the GRAIL antenna calibration on 2 March 2012. Displayed are (a) the computed (expected) signature in the range residual and the observed signature after fitting the range residuals using the GL0420A gravity field, and (b) the observed signature for preliminary gravity fields developed during the Primary Mission with progression toward higher degree (210, 270, 360, and 420) showing the improvement in matching the expected signature.

LP nominal mission are similar for both models, and it may be possible to improve the fits by combining LP data with GRAIL data in the gravity solution. However, this may not be necessary as the processing of the GRAIL primary and extended missions improves. The LP orbit solutions for the extended mission at lower altitude will definitely benefit from the processing of the GRAIL extended mission data, since LP RMS fits occasionally increase when using GL0660B to degree higher than $n = 360$. The improvement in the gravity field can be also assessed by the LP orbit overlap differences. For the entire LP nominal mission of 148 orbit overlaps, the LP150Q average overlap errors in the radial, along-track, and orbit normal directions (or RTN) are 0.3, 3.5, and 2.6 m (slightly better than the ~5 m of *Carranza et al.* [1999] using an older LP100J model) and GL0660B has a similar 0.3, 3.4, and 3.1 m. Since GL0660B does not contain LP data, it may be possible to fine-tune low-degree terms for the LP orbit. For the lower altitude LP extended mission of 100 orbit overlaps, the overlaps are noticeably improved by ~3× from LP150Q errors of 1.7, 23.8, and 18.1 m (smaller than ~100 m of *Carranza et al.*, 1999) to GL0660B errors of 0.9, 8.3, and 4.8 m. GRAIL extended mission data at lower altitude will further improve orbit determination especially at lower altitudes.

[66] The GRAIL Level-1 process requires accurately determined GRAIL orbits to avoid orbit geometry errors in the generation of the KBRR data. The initial orbit determination error based upon the LP150Q gravity model was ~100 m, consistent with LP errors for low altitude orbits [*Carranza et al.*, 1999]. The orbit overlap errors for both GRAIL spacecraft during the PM are now less than one meter in all three directions (radial, along-track, and orbit normal) using the GL0660B gravity field (see Figure 20). The overlap errors are shown for two fields with different assumptions on the empirical acceleration model, a uniform 10^{-11} km/s^2 a priori amplitude and the variable amplitude based upon the spacecraft thermal acceleration magnitude as used by GL0660B. The looser a priori seems to slightly help orbit solutions for a few dates, but the variable method gives slightly more consistent Love number solutions. We chose the variable periodic model because it follows what is expected from the thermal model.

[67] An offset for the measurement time (barycentric dynamical time or TDB) of the KBRR observable is estimated as a bias for every GRAIL data arc. In the initial processing of the PM KBRR data, the time tag offset could vary by up to 50 ms between arcs due to errors in the a priori values of the GRAIL timing system. However, once the times between the two GRAIL spacecraft clocks and DSN were calibrated in the Level-1 process (the version 2 KBRR data), the overall absolute time tag accuracy of the KBRR observable is ~1 μs, and this bias should remain constant for the duration of the PM to ~10^{-8} s [*Kruizinga et al.*, 2013]. The solutions for the time tag using GL0660B show a RMS scatter of 110 μs, about 40× the formal uncertainties of 2–6 μs (similar to scaling of errors for low-degree gravity and Love number). Future gravity determination efforts will estimate only one time tag bias for the duration of the PM to avoid introducing errors into the long wavelength gravity parameters.

[68] During the PM the GRAIL spacecraft performed attitude maneuvers to calibrate the vector from the center-of-mass to the Ka-band antenna phase center (or boresight) for each spacecraft. The calibrations occurred on 8 and 9 March, 3 April, and 2 and 29 May, where each calibration involved a series of nonpropulsive maneuvers to tilt the boresight vector by 3° using the attitude reaction wheels. The calibration starts with three boresight slews up and down relative to the interspacecraft range vector to change the spacecraft range distance by ~1.5 mm, followed by a quiet period of 5 min, and then the three slews repeated. The range residuals from processing of the Ka-band range data during the calibration proved to be an excellent test of both the long and short wavelength errors of the gravity field. As an example, Figure 21a shows the 2 March calibration for GRAIL-A at a 29-km altitude. Both the expected range residual behavior (assuming all orbit and hence gravity error has been removed) and the corresponding range residuals from the GL0420A gravity field are displayed showing a good match. The progression of the gravity field improvement (as indicated by higher numbers or higher harmonic degree) during the PM is evident in Figure 21b.

8. Summary

[69] The GRAIL mission Ka-band interspacecraft range-rate data from the Primary Mission have unprecedented

accuracy near 0.03 μm/s, about 4 orders-of-magnitude improvement versus previous DSN based S-band tracking missions to the Moon. As a result, the gravity field of the Moon shows similar improvement for nearly all harmonic wavelengths and more than 5 orders-of-magnitude for some frequencies, resulting in new discoveries about the lunar interior from crust to core. The lunar gravity derived from GRAIL reveals strong 98% coherence with topography [*Zuber et al*., 2013b], crustal fractures likely from an early thermal expansion of the Moon [*Andrews-Hanna et al*., 2013], and lower crustal density and higher porosity than previously thought [*Wieczorek et al*., 2013]. The interior of the Moon is also constrained by new moments of inertia from improved long-wavelength gravity harmonics, a ~5× improved lunar k_2 Love number (*Williams et al*., submitted manuscript, 2013), and also the first detection of the k_3 Love number. The gravity field based upon only the GRAIL PM also demonstrates improved spacecraft orbit accuracy for past and future missions. However, the full benefit from the GRAIL mission is yet to come. With processing of the lower-altitude extended mission, the expected gravity resolution should double that of the PM, leading to additional science discoveries and lunar navigation improvement.

[70] **Acknowledgments.** The research described in this paper was carried out at the Jet Propulsion Laboratory, California Institute of Technology, under contract with the National Aeronautics and Space Administration. We gratefully acknowledge the use of the Lonestar Texas Supercomputer used in the initial development of the GRAIL lunar gravity field and the Ames Pleiades Supercomputer that was used to generate the GL0660B gravity solution of this paper. We thank the GRAIL Navigation team (P. Antresian, M. Ryne, T. You) for many useful discussions and feedback on the GRAIL gravity fields, and for the Mission Design team (R. Roncoli, M. Wallace, S. Hatch, T. Sweetser) for accommodating many of the requests to optimize the gravity science. We thank K. Oudrhiri, D. Kahan, and D. Fleischman for their GRAIL Level-1 contributions, and W. Lu for earlier contributions to the GRAIL gravity effort.

References

Akim, E. L. (1966), Determination of the Gravitational Field of the Moon from the Motion of the Artificial Lunar Satellite "Lunar-10", *Dokl. Akad. Nauk SSSR*, *170*, 799–802.

Andrews-Hanna, J. C., et al. (2013), Ancient igneous intrusions and the early expansion of the Moon revealed by GRAIL gravity gradiometry, *Science*, *339*, doi:10.1126/science.1231753.

Archinal, B. A., et al. (2011), Report of the IAU Working Group on Cartographic Coordinates and Rotational Elements: 2009, *Celestial Mech. Dyn. Astron.*, *109*, 101–135.

Asmar, S. W., et al. (2013), The scientific measurement system of the Gravity Recovery and Interior Laboratory (GRAIL) mission, *Space Sci. Rev.*, *174*, doi:10.1007/s11214-013-9962-0.

Bierman, G. J. (1977), *Factorization Methods for Discrete Sequential Estimation*, Academic Press, New York.

Bills, B. G., and A. J. Ferrari (1980), A Harmonic Analysis of Lunar Gravity, *J. Geophy. Res.*, *85*, 1013–1025.

Carranza, E., A. Konopliv, and M. Ryne (1999), *Lunar Prospector Orbit Determination Uncertainties Using the High Resolution Lunar Gravity Models, AAS Paper 99–325*, AAS/AIAA Astrodynamics Specialist Conference, Girdwood, Alaska, August, 1999.

Dickey, J. O., et al. (1994), Lunar Laser Ranging: A Continuing Legacy of the Apollo Program, *Science*, *265*, 482–490.

Fahnestock, E. G., R. S. Park, D.-N. Yuan, and A. S. Konopliv (2012), *Spacecraft Thermal And Optical Modeling Impacts on Estimation of the GRAIL Lunar Gravity Field*, AIAA/AAS Astrodynamics Specialist Conference, August 13–16, 2012, Minneapolis, Minn., AIAA, 2012-4428.

Floberhagen, R., P. Visser, and F. Weischede (1999), Lunar albedo forces modeling and its effect on low lunar orbit and gravity field determination, *Adv. Space Res.*, *23*, 733–378.

Goossens, S., et al. (2011), Lunar gravity field determination using SELENE same-beam differential VLBI tracking data, *J. Geod.*, *85*, 205–228, doi:10.1007/s00190-010-0430-2.

Han, S.-C., E. Mazarico, D. Rowlands, F. Lemoine, and S. Goossens (2011), New analysis of Lunar Prospector radio tracking data brings the nearside gravity field of the Moon with an unprecedented resolution, *Icarus*, *215*, 455–459, doi:10.1016/j.icarus.2011.07.020.

Harvey, N., E. Fahnestock, D. Kahan, A. Konopliv, G. Kruizinga, K. Oudrhiri, M. Paik, D. Yuan, S. Asmar, and M. Watkins (2012), *GRAIL Level-1 Algorithm Theoretical Basis Document, JPL D-75862*, Jet Propulsion Laboratory, California Institute of Technology, Pasadena, Calif.

Heiskanen, W. A., and H. Moritz (1967), *Physical Geodesy*, W. H. Freeman and Company, San Francisco and London.

Kaula, W. M. (1966), *Theory of Satellite Geodesy*, Blaisdell, Waltham, MA.

Kim, J. R. (2000), *Simulation Study of a Low-Low Satellite-to-Satellite Tracking Mission*, Ph.D. Dissertation, University of Texas at Austin, May 2000.

Klipstein, W. M., B. W. Arnold, D. G. Enzer, A. A. Ruiz, J. Y. Yien, R. T. Wang, and C. E. Dunn (2013), The Lunar Gravity Ranging System for the Gravity Recovery and Interior Laboratory (GRAIL) Mission, *Space Sci. Rev.*, doi:10.1007/s11214-013-9973-x.

Konopliv, A. S., W. L. Sjogren, R. N. Wimberly, R. A. Cook, and A. Vijayaraghavan (1993), *A High Resolution Lunar Gravity Field and Predicted Orbit Behavior*, AAS Paper 93–622, AAS/AIAA Astrodynamics Specialist Conference, Victoria, B.C., Can., August, 1993.

Konopliv, A. S., A. B. Binder, L. L. Hood, A. B. Kucinskas, and J. G. Williams (1998), Improved Gravity Field of the Moon from Lunar Prospector, *Science*, *281*, 1476–1480.

Konopliv, A. S., W. B. Banerdt, and W. L. Sjogren (1999), Venus Gravity: 180th Degree and Order Model, *Icarus*, *139*, 3–18.

Konopliv, A. S., S. W. Asmar, E. Carranza, W. L. Sjogren, and D.-N. Yuan (2001), Recent Gravity Models as a Result of the Lunar Prospector Mission, *Icarus*, *150*, 1–18.

Konopliv, A. S., S. W. Asmar, W. M. Folkner, O. Karatekin, D. C. Nunes, S. E. Smrekar, C. F. Yoder, and M. T. Zuber (2011), Mars High Resolution Gravity Fields from MRO, Mars Seasonal Gravity, and Other Dynamical Parameters, *Icarus*, *211*, 401–428.

Krogh, F. T. (1973), *Changing Stepsize in the Integration of Differential Equations Using Modified Divided Differences, JPL Tech. Mem. No. 312, Section 914* (internal document), Jet Propulsion Laboratory, California Institute of Technology, Pasadena, Calif.

Kruizinga, G., W. Bertiger, and N. Harvey (2012), *Timing of Science Data for the GRAIL Mission, JPL D-75620*, Jet Propulsion Laboratory, California Institute of Technology, Pasadena, Calif.

Kruizinga, G., et al. (2013), The role of grail orbit determination, in *Preprocessing of Gravity Science Measurements*, AAS 13–270, 23rd AAS/AIAA Space Flight Mechanics Meeting, Kauai, Haw., February, 2013.

Lambeck, K. (1988), *Geophysical Geodesy*, Clarendon Press, Oxford.

Lawson, C. L., and R. J. Hanson (1995), *Solving Least Squares Problems, SIAM Classics in Applied Mathematics*, vol. 15, Society for Industrial and Applied Mathematics, Philadelphia, Pa.

Lemoine, F. G., D. E. Smith, M. T. Zuber, G. A. Neumann, and D. D. Rowlands (1997), A 70th Degree Lunar Gravity Model (GLGM-2) from Clementine and Other Tracking Data, *J. Geophys. Res.*, *102*, 16,339–16,359.

Lemoine, F. G., et al. (2013), High degree gravity models from GRAIL Primary mission data, *J. Geophys. Res. Planets*, doi:10.1016/j.epsl.2012.12.021.

Matsumoto, K., et al. (2010), An improved lunar gravity field model from SELENE and historical tracking data: Revealing the farside gravity features, *J. Geophys. Res.*, *115*, E06007, doi:10.1029/2009JE003499.

Mazarico, E., F. G. Lemoine, S.-C. Han, D. E. Smith (2010), GLGM-3: A degree 150 lunar gravity model from the historical tracking data of NASA Moon orbiters, *J. Geophys. Res.*, *115*, E05001, doi:10.1029/2009JE003472.

McCarthy, D. D., and G. Petit (eds.) (2003), *IERS Conventions, IERS Technical Note, 32*.

Moyer, T. D. (1971), *Mathematical Formulation of the Double-Precision Orbit Determination Program (DPODP), JPL Technical Report 32–1527*, Jet Propulsion Laboratory, California Institute of Technology, Pasadena, Calif.

Moyer, T. D. (2003), *Formulation for Observed and Computed Values of Deep Space Network Data Types for Navigation*, John Wiley & Sons, Hoboken, N.J.

Muller, P. M., and W. L. Sjogren (1968), Mascons: Lunar Mass Concentrations, *Science*, *161*, 680–684.

Namiki, N., et al. (2009), Farside gravity field of the Moon from four-way Doppler measurements of SELENE (Kaguya), *Science*, *323*, 900–905, doi:10.1126/science.

Park, R. S., S. W. Asmar, E. G. Fahnestock, A. S. Konopliv, W. Lu, and M. M. Watkins (2012), Gravity Recovery and Interior Laboratory Simulations of Static and Temporal Gravity Field, *J. Spacecraft and Rockets*, *49*, 390–400.

Roncoli, R., and K. Fujii (2010), *Mission Design Overview for the Gravity Recovery and Interior Laboratory (GRAIL) Mission, AIAA Guidance*,

Navigation, and Control Conference, August 2010, Toronto, Ontario Canada, AIAA 2010–8383.

Smith, D. E., et al. (2010), Initial observations from the Lunar Orbiter Laser Altimeter (LOLA), *Geophys. Res. Lett.*, *37*, L18204, doi:10.1029/2010GL043751.

Tapley, B. D., S. Bettadpur, J. C. Ries, P. F. Thompson, and M. M. Watkins (2004a), GRACE measurements of mass variability in the Earth system, *Science*, *305*, 503–505, doi:10.1126/science.1099192.

Tapley, B. D., B. E. Schutz, and G. H. Born (2004b), *Statistical Orbit Determination*, Elsevier, Boston, Mass.

Weber, R. C., P.-Y. Lin, E. J. Garnero, Q. Williams, and P. Lognonne (2011), Seismic detection of the lunar core, *Science*, *331*, 309–312, doi:10.1126/science.1199375.

Wieczorek, M. A., and R. J. Phillips (1998), Potential anomalies on a sphere: Applications to the thickness of the lunar crust, *J. Geophys. Res.*, *103*(E1), 1715–1724.

Wieczorek, M. A., et al. (2013), The crust of the Moon as seen by GRAIL, *Science*, *339*, doi:10.1126/science.1231530.

Williams, J. G. (2007), A scheme for lunar inner core detection, *Geophys. Res. Lett.*, *34*, L03202, doi:10.1029/2006GL028185.

Williams, J. G. (2012), *Lunar potential's tidal dissipation terms, JPL IOM 335-JGW-20120228-005, February 28, 2012 (internal document)*, Jet Propulsion Laboratory, California Institute of Technology, Pasadena, CA.

Williams, J. G., D. H. Boggs, and W. M. Folkner (2008), *DE421 Lunar Orbit, Physical Librations, and Surface Coordinates, JPL IOM 335-JW, DB, WF-20080314-001, March 14, 2008* (internal document), Jet Propulsion Laboratory, California Institute of Technology, Pasadena, Calif.

Zuber, M. T., D. E. Smith, F. G. Lemoine, and G. A. Neumann (1994), The shape and internal structure of the Moon from the Clementine mission, *Science*, *266*, 1839–1843.

Zuber, M. T., D. E. Smith, D. H. Lehman, T. L. Hoffman, S. W. Asmar, and M. M. Watkins (2013a), Gravity Recovery and Interior Laboratory (GRAIL): Mapping the lunar interior from crust to core, *Space Sci. Rev.*, *174*, doi:10.1007/s11214-012-9952-7.

Zuber, M. T., et al. (2013b), Gravity field of the Moon from the Gravity Recovery and Interior Laboratory (GRAIL) mission, *Science*, *339*, doi:10.1126/science.1231507.